

Characterisation of the warm-Jupiter TOI-1130 system with CHEOPS and a photo-dynamical approach[★]

L. Borsato¹, D. Degen², A. Leleu^{3,4}, M. J. Hooton⁵, J. A. Egger⁴, A. Bekkelien³, A. Brandeker⁶, A. Collier Cameron⁷, M. N. Günther⁸, V. Nascimbeni¹, C. M. Persson⁹, A. Bonfanti¹⁰, T. G. Wilson¹¹, A. C. M. Correia¹², T. Zingales^{13,1}, T. Guillot¹⁴, A. H. M. J. Triaud¹⁵, G. Piotto^{1,13}, D. Gandolfi¹⁶, L. Abe¹⁴, Y. Alibert^{17,4}, R. Alonso^{18,19}, T. Bączny²⁰, D. Barrado Navascues²¹, S. C. C. Barros^{22,23}, W. Baumjohann¹⁰, T. Beck⁴, P. Bendjoya¹⁴, W. Benz^{4,17}, N. Billot³, C. Broeg^{4,17}, M.-D. Busch²⁴, Sz. Csizmadia²⁵, P. E. Cubillos^{10,26}, M. B. Davies²⁷, M. Deleuil²⁸, A. Deline³, L. Delrez^{29,30,31}, O. D. S. Demangeon^{22,23}, B.-O. Demory^{17,4}, A. Deras³², B. Edwards³³, D. Ehrenreich^{3,34}, A. Erikson²⁵, A. Fortier^{4,17}, L. Fossati¹⁰, M. Fridlund^{35,9}, K. Gazeas³⁶, M. Gillon²⁹, M. Güdel³⁷, A. Heitzmann³, Ch. Helling^{10,38}, S. Hoyer²⁸, K. G. Isaak⁸, L. L. Kiss^{39,40}, J. Korth⁴¹, K. W. F. Lam²⁵, J. Laskar⁴², A. Lecavelier des Etangs⁴³, M. Lendl³, D. Magrin¹, L. Marafatto¹, P. F. L. Maxted⁴⁴, M. Mecina³⁷, D. Mékarnia¹⁴, C. Mordasini^{4,17}, D. Mura^{45,46}, G. Olofsson⁶, R. Ottensamer³⁷, I. Pagano⁴⁷, E. Pallé^{18,19}, G. Peter⁴⁸, D. Pollacco¹¹, D. Queloz^{2,5}, R. Ragazzoni^{1,13}, N. Rando⁸, F. Ratti⁸, H. Rauer^{25,49}, I. Ribas^{50,51}, S. Salmon³, N. C. Santos^{22,23}, G. Scandariato⁴⁷, D. Ségransan³, A. E. Simon^{4,17}, A. M. S. Smith²⁵, S. G. Sousa²², M. Stalport^{30,29}, O. Suarez¹⁴, S. Sulis²⁸, Gy. M. Szabó^{32,52}, S. Udry³, V. Van Grootel³⁰, J. Venturini³, E. Villaver^{18,19}, N. A. Walton⁵³, and D. Wolter²⁵

(Affiliations can be found after the references)

Received 3 June 2024 / Accepted 6 July 2024

ABSTRACT

Context. Among the thousands of exoplanets discovered to date, approximately a few hundred gas giants on short-period orbits are classified as ‘lonely’ and only a few are in a multi-planet system with a smaller companion on a close orbit. The processes that formed multi-planet systems hosting gas giants on close orbits are poorly understood, and only a few examples of this kind of system have been observed and well characterised.

Aims. Within the context of a multi-planet system hosting a gas giant on short orbits, we characterise the TOI-1130 system by measuring masses and orbital parameters. This is a two-transiting planet system with a Jupiter-like planet (c) on a 8.35 days orbit and a Neptune-like planet (b) on an inner (4.07 days) orbit. Both planets show strong anti-correlated transit timing variations (TTVs). Furthermore, radial velocity (RV) analysis showed an additional linear trend, a possible hint of a non-transiting candidate planet on a far outer orbit.

Methods. Since 2019, extensive transit and radial velocity observations of the TOI-1130 have been acquired using TESS and various ground-based facilities. We present a new photo-dynamical analysis of all available transit and RV data, with the addition of new CHEOPS and ASTEP+ data, which achieve the best precision to date on the planetary radii and masses and on the timings of each transit.

Results. We were able to model interior structure of planet b constraining the presence of a gaseous envelope of H/He, while it was not possible to assess the possible water content. Furthermore, we analysed the resonant state of the two transiting planets, and we found that they lie just outside the resonant region. This could be the result of the tidal evolution that the system underwent. We obtained both masses of the planets with a precision of less than 1.5%, and radii with a precision of about 1% and 3% for planet b and c, respectively.

Key words. methods: data analysis – methods: observational – techniques: photometric – telescopes – planetary systems

1. Introduction

Among the more than 5500¹ confirmed exoplanets, about 500 are classified as ‘lonely’ hot Jupiters (HJs, Latham et al. 2011; Steffen et al. 2012; Huang et al. 2016; Schlaufman & Winn 2016), that is gas giants on short orbital periods. Of those, only a

few are part of multi-planet systems hosting smaller companions on close (inner) orbits, for example WASP-47 (Hellier et al. 2012; Becker et al. 2015; Bryant & Bayliss 2022; Nascimbeni et al. 2023), Kepler-730 (Zhu et al. 2018; Cañas et al. 2019), TOI-5398 (Mantovan et al. 2022, 2024), and, the subject of this work, TOI-1130 (Huang et al. 2020a; Korth et al. 2023). However the definition of HJ is not so strict, and it sometimes overlaps with warm Jupiter (WJ) exoplanets, gas giants with periods of ~8–200 d (Huang et al. 2016). These WJs show different orbital configurations compared with HJs, as Huang et al.

[★] This study uses CHEOPS data observed as part of the Guaranteed Time Observation (GTO) programmes CH_PR00015, CH_PR00031, and CH_PR00053.

¹ NASA Exoplanet Archive at 2024-04-22.

(2016) found that about 50% of the *Kepler* sample of WJs are in multi-planet systems. This led to it being inferred that the formation and evolution processes (Wu et al. 2018; Kley 2019) of WJ and HJ are different. The characterisation of gas-giant systems enables us to ascertain which migration process the system underwent: disk-driven migration (Lin et al. 1996; Baruteau et al. 2016) or high-eccentricity migration (HEM, Rasio & Ford 1996; Chatterjee et al. 2008; Nagasawa et al. 2008). It has been suggested by Vick et al. (2019, 2023) and Jackson et al. (2023) that the main process forming HJs is the HEM, while there is no clear hint of a dominant mechanism forming WJ systems (Borsato et al. 2021).

We decided to observe TOI-1130 (Huang et al. 2020a; Korth et al. 2023) a two-transiting planet system hosting a gas giant TOI-1130 c on an 8 d period orbit, and a lower-mass planet, TOI-1130 b, on an inner orbit ($P_b \sim 4$ d), and a linear trend in the radial velocity data could be a hint of an additional candidate planet on a far outer orbit. We collected (see Sect. 2) published transit and radial velocity (RV) data and new transit observations with the CHAracterising ExOPlanet Satellite (CHEOPS, Benz et al. 2021) and ASTEP+ (Schmider et al. 2022), and an additional sector of the Transiting Exoplanet Survey Satellite (TESS; Ricker et al. 2015). We updated the stellar parameters (Sect. 3) and we improved the radii measurement, masses, and the architecture of the planets through the analysis of transit time variation (TTV) signals (Agol et al. 2005; Holman & Murray 2005; Steffen et al. 2012) with a photo-dynamical approach (Sect. 4) on a data set almost two years longer than Korth et al. (2023). We finally present the results in Sect. 5 and in Sect. 6 we compare them with the work of Korth et al. (2023) and draw our conclusions.

2. Observations

2.1. Photometry

2.1.1. CHEOPS

TOI-1130 has been observed with CHEOPS within three GTO programmes for a total of 17 light curves (see Table A.1 for the full list of the CHEOPS observations). In particular, planet b has been observed in 11 visits, initially within the programme *CHESS*² and later in the programme *System Architecture*³. We collected six CHEOPS visits of TOI-1130 c, which was part of the GTO programme *Companion to Warm Jupiter planets TTV*⁴ (Borsato et al. 2021) and also of the *System Architecture* programme. For each visit we extracted the aperture photometry with the default aperture of 25 pixels provided by the DRP 14.1 (Hoyer et al. 2020). After each observation we analysed as single-visit the data with PYCHEOPS (Maxted et al. 2022), with priors on the transit parameters based on the discovery paper (Huang et al. 2020a) and we determined the detrending parameters using the Bayes Factor, as described in Maxted et al. (2022). This allowed us to update our linear ephemeris improving our prediction of the transit times and constraining the observations with CHEOPS. However, due to the large TTV of both planets, in the visit of planet c on 21 June 2022 (CHEOPS visit num. 14 in Table. A.1) the post-transit shows an additional transit-like feature that, after many attempts to correct it, we attributed it to planet b.

² CHEOPS GTO PR-100031, M. Hooton.

³ CHEOPS GTO PR-120053, A. Leleu.

⁴ CHEOPS GTO PR-100015, G. Piotto & L. Borsato.

2.1.2. TESS

TOI-1130 has been observed by the TESS (Ricker et al. 2015) in three sectors: 13, 27, and 67 (see Table A.1). For sector 13 (S13), we used the already flattened KSPSAP_FLUX light curve from the Quick Look Pipeline (QLP; Huang et al. 2020b), while for sectors 27 (S27) and 67 (S67), we used the Presearch Data Conditioned Simple Aperture Photometry (PDCSAP) light curves (in the 20 s fast mode), as processed by the Science Processing Operation Center (SPOC; Jenkins et al. 2016).

2.1.3. Ground-based photometry

The ground-based observations used in our analysis were taken by six ground-based telescopes, namely ASTEP⁵, CDK14⁶, PEST⁷, LCO-CTIO⁸, LCO-SSO⁹, and LCO-SAAO¹⁰ from the Las Cumbres Observatory (LCO). The observations we used are largely the same as those used by Korth et al. (2023) with four differences that will be discussed here. Firstly, we decided to include the observations of ASTEP (0.4 m) and PEST (0.3 m) in addition to the observation of LCO-SSO (1 m) of the same transit of planet c on 5 August 2020. Secondly, we fitted for transits of both planet b and planet c in the observation of LCO-CTIO on the 26th of June 2021, while Korth et al. (2023) do not report to have used the transit of planet b from this observation. Thirdly, we did not take into account the observation of planet b from LCOGT-SAAO on 7 October 2021, as this transit was observed simultaneously by CHEOPS. Given that the CHEOPS photometric precision is far greater than that of LCOGT-SAAO, and the fact that all contact points of this transit were well constrained by CHEOPS' observation, the inclusion of this data would unnecessarily complicate the analysis. Lastly, we did not use LCOGT-CTIO's observation of planet b on 8 October 2021, as it contained more red noise than any other ground-based observation and was the only data set for which no cotrending basis vectors were provided at the time of analysis. In summary, we used 19 ground-based telescope observations, encompassing 6 transits of planet b and 10 transits of planet c. A more detailed description of the data selection and processing is given in Degen (2022).

We also obtained photometric observation with ASTEP+ (Guillot et al. 2015), taking advantage of the new camera system with simultaneous observations in two bands, ASTEP+B between 400 and 700 nm and ASTEP+R between 700 and 1000 nm (see Schmider et al. 2022). We observed two transits of planet b and three of planet c (see observation log in Table A.1), for a total of 10 light curves. The data analysis was performed using aperture photometry, as described in Mékarnia et al. (2016). For each light curve we also have some diagnostics, that is, $X - Y$ coordinates on the CCD, FWHM, the sky background, and the airmass.

2.2. Radial velocities

We collected all the radial velocities (RVs) available in literature, 21 RVs with CHIRON (Tokovinin et al. 2013) from the discovery paper by Huang et al. (2020a), 49 RVs from HARPS

⁵ Antarctic Search for Transiting Exoplanets.

⁶ El Sauce Observatory in Chile.

⁷ Perth Exoplanet Survey Telescope, backyard observatory in western Australia.

⁸ Cerro Tololo Interamerican Observatory in Chile.

⁹ South at Siding Spring Observatory in eastern Australia.

¹⁰ South African Astronomical Observatory.

Table 1. Results from the spectroscopic stellar modelling of TOI-1130.

	This work			
	SpecMatch-Emp	SME	H20 ^(a)	K23 ^(b)
T_{eff} (K)	4256 ± 70	4360 ± 108	4250 ± 67	4350 ± 60
log g_{\star} (cgs)	4.65 ± 0.12	4.55 ± 0.07	4.60 ± 0.02	4.62 ± 0.04
[Fe/H] (dex)	0.17 ± 0.09	0.11 ± 0.10	>0.2	0.30 ± 0.06
[Si/H] (dex)	...	0.12 ± 0.11
[Mg/H] (dex)	...	0.13 ± 0.12
$V \sin i$ (km s ⁻¹)	...	2.5 ± 0.9	4.0 ± 0.5	≤3
M_{\star} (M_{\odot})	...	0.722 ^{+0.042} _{-0.037}	0.684 ^{+0.016} _{-0.017}	0.71 ± 0.02
R_{\star} (R_{\odot})	...	0.697 ± 0.011	0.687 ± 0.015	0.68 ± 0.02
ρ_{\star} (ρ_{\odot})	...	2.13 ± 0.16	2.11 ± 0.15	2.12 ± 0.15
t_{\star} (Gyr)	...	5.4 ^{+5.7} _{-4.9}	8.2 ^{+3.8} _{-4.9}	3.2–5

References. ^(a)Huang et al. (2020a); ^(b)Korth et al. (2023).

(Mayor et al. 2003) and 20 from PFS (Crane et al. 2006, 2008, 2010) published by Korth et al. (2023).

3. Stellar parameters

We utilised our co-added high-resolution HARPS spectra ($R = 115\,000$) to perform spectroscopic modelling of TOI-1130. We began by running the empirical SpecMatch-Emp (Yee et al. 2017) software which compares a library of well-characterised stars to our observations. The results indicate that the star is a K6 V star. We compared the outcome with Spectroscopy Made Easy¹¹ (SME; Valenti & Piskunov 1996; Piskunov & Valenti 2017) which fits observations to compute synthetic spectra from stellar atmosphere grids and atomic and molecular line data from VALD (Ryabchikova et al. 2015). For modelling of TOI-1130, we chose the MARCS model atmosphere (Gustafsson et al. 2008), and verified the results with the Atlas12 atmosphere grid (Kurucz 2013). We fixed the micro- and macro-turbulent velocities, V_{mic} and V_{mac} , to 0.1 km s⁻¹ and 1.0 km s⁻¹ (Gray 2008). The modelling steps are described in Persson et al. (2018).

Even though mid-K stars and later are often challenging to model with spectral synthesis software, the results of the final SME model are in very good agreement with Specmatch-emp. The results from both models are listed in Table 1. We started from both these two sets of outcomes to derive the isochronal parameters of the star (see below) and we found that the SME-based data enable us to compute a more precise stellar mass. Therefore, we assumed the SME-based spectroscopic parameters as the reference values of this work.

To determine the stellar radius of TOI-1130 we used an MCMC modified infrared flux method (Blackwell & Shallis 1977; Schanche et al. 2020). Using spectral energy distributions (SEDs) built from stellar atmospheric models (Castelli & Kurucz 2003) with priors coming from our spectral analysis, we computed synthetic photometry that we compared to observed broadband photometry in the following band-passes: *Gaia* G , G_{BP} , and G_{RP} , 2MASS J , H , and K , and *WISE* $W1$ and $W2$ (Skrutskie et al. 2006; Wright et al. 2010; Gaia Collaboration 2023). Using the derived stellar bolometric flux and known physical relations, we determined the effective temperature and angular diameter of TOI-1130 that we translated into stellar radius using the offset-corrected *Gaia* parallax (Lindgren et al. 2021) to $R_{\star} = 0.697 \pm 0.011 R_{\odot}$.

We used T_{eff} , [Fe/H], and R_{\star} along with their uncertainties as the basic set of input parameters to then derive the isochronal mass M_{\star} and age t_{\star} by employing two different sets

¹¹ <http://www.stsci.edu/~valenti/sme.html>

of stellar evolutionary models. In detail, we computed a first pair of mass and age estimates via the CLES code (Code Liègeois d'Évolution Stellaire; Scufflaire et al. 2008), which generates the best stellar evolutionary track ‘on-the-fly’ accounting for the input parameters and following the Levenberg-Marquadt minimisation scheme (Salmon et al. 2021). For the second pair of estimates, instead, we utilised the isochrone placement algorithm (Bonfanti et al. 2015, 2016), which interpolates the input values within pre-computed grids of PARSEC¹² v1.2S (Marigo et al. 2017) isochrones and tracks. As the isochrone placement implements also the gyrochronological relation by Barnes (2010) to work in synergy with isochrone fitting (see Bonfanti et al. 2016), we further inputted $v \sin i$ to improve convergence. We finally checked the mutual consistence of the two respective pairs of outcomes via the χ^2 -based criterion outlined in Bonfanti et al. (2021) and combined the results obtaining $M_{\star} = 0.722^{+0.042}_{-0.037} M_{\odot}$ and $t_{\star} = 5.4^{+5.7}_{-4.9}$ Gyr, and a stellar density of $\rho_{\star} = 2.13 \pm 0.16 \rho_{\odot}$.

4. Data analysis and modelling

For each TESS sector we discarded data points with QUALITY factor greater than 0 and with flux 10- σ above the median flux. We then selected a portion of the light curve around each transit of both planets, taking into account the transit duration and at least the equivalent of three CHEOPS orbits (about 98.77 minutes each). We sought the transits through the linear ephemeris and transit parameter by Huang et al. (2020a), and we visually checked if the transit was missed due to the predicted TTV and we adjusted the centre of the portion if needed. In one case we had to join a planet b and c transit because the two portions were too close to keep them separated. We repeated the same procedure and portioned S67 with updated linear ephemeris from Korth et al. (2023) and CHEOPS data.

As the results of the shallow transit of b and of the gaps in the CHEOPS visits, during the preliminary single-visit analysis we found that the planetary parameters did not agree visit-by-visit. Given the high number¹³ of parameters needed to perform an MCMC analysis of a simultaneous fit of the transits and the detrending parameters for each light curve, we decided to inspect which are the common diagnostics across all the light curves. Plotting as function of the roll angle (ϕ) the different diagnostics, we found that the position on the CCD ($x - y$ offset), and its second derivative, could be treated as common parameters across all the visits. We also modelled the roll angle with a common sinusoidal with six harmonics. While a flux constant, a linear and quadratic term in time, the background, and the ramp effect (see Maxted et al. 2022) were defined visit-by-visit. We masked all the portions of the transits in the light curves, we performed a PYCHEOPS detrending-like least-squares¹⁴ fit of all the visits simultaneously. We also extract the ‘‘PSF imagerie photometric extraction’’ (PIPE) package¹⁵ photometry, that is less prone to contamination and background effects (Morris et al. 2021; Brandeker et al. 2022). We apply the same full-detrending,

¹² Padova and TRieste Stellar Evolutionary Code: <http://stev.oapd.inaf.it/cgi-bin/cmd>

¹³ When detrending 17 CHEOPS light curves, more than 90 parameters are required, with approximately 11 common parameters and 5 per visit. Taking into account all the photometries, radial velocity data sets, stellar parameters, and orbital parameters we could have more than 250 parameters.

¹⁴ Levenberg-Marquardt algorithm of MINPACK (Moré et al. 1980) implemented in `scipy.optimize.leastsq`

¹⁵ <https://github.com/alphapsa/PIPE>

after masking the transits. We repeated this analysis with and without the last CHEOPS visit with planet c and b (hereafter V14). We found that V14 cannot be detrended in such way, so we kept the analysis without it. We also found that the PIPE photometry provided a median out-of-transit standard deviation $\sigma_{\text{phot,PIPE}} = 552 \pm 23$ ppm, lower than DPR case with $\sigma_{\text{phot,DRP}} = 659 \pm 58$ ppm. For this reason, in following analysis we decided to use 16 pre-detrended visits from PIPE photometry out of 17, and the V14 from PIPE without pre-detrending.

4.1. Ground-based photometry

Ground-based observations generally exhibit higher levels of both white and red noise than space telescopes, mainly due to atmospheric turbulence. Reducing the effect of these systematic errors requires the introduction of detrending parameters, thereby increasing the dimension of the parameter space. The increase in dimensionality not only increases the computational complexity but also makes statistical inference challenging, for example by slowing convergence and introducing degeneracies, thus limiting the comprehensive exploration of the parameter space and, therefore, the reliable extraction of meaningful information. For these reasons, we decided to prioritise precision over quantity and split the analysis into two phases: first, a photometric analysis of the ground-based telescope data to extract the transit times of the planets, and then a photo-dynamic analysis of the space telescope data. In this way, we are able to incorporate the transit times obtained from the ground-based telescope data into the photo-dynamic analysis without inflating the dimension of the parameter space of the main analysis by more than 100 parameters that were identified as useful for detrending the ground-based telescope data by the Bayesian information criterion. In the following subsection we give a brief overview of the analysis of the ground-based telescope data, which is described in more detail in [Degen \(2022\)](#).

We performed two photometric analyses, each combining the ground-based observations with data from TESS sectors 13 and 27. The difference between the two analyses lay in the strictness with which we discarded flux measurement points as outliers, which was done on the basis on their absolute deviation from the local median with a width size of 11. The two TESS sectors were included to constrain nuisance parameters, in particular the planetary radii, and, thus, reduce the uncertainty in the extracted transit times. The analyses were performed using the python package EXOPLANET ([Foreman-Mackey et al. 2021a,b](#)) and its dependencies ([Agol et al. 2020](#); [Kumar et al. 2019](#); [Astropy Collaboration 2013, 2018](#); [Luger et al. 2019](#); [Salvatier et al. 2015](#); [Theano Development Team 2016](#)). PYMC3 ([Salvatier et al. 2015](#)) served as the inference engine, employing the No U-Turn Sampler (NUTS) for efficient posterior exploration. Convergence was assessed using Gelman-Rubin diagnostics, trace plots, and corner plots.

We restricted our analyses from small to moderate eccentricities (<0.2), so we should remain unaffected from the divergent errors that the modified Newton-Raphson method used by this package has been shown to have at large eccentricities ([Tommasini & Olivieri 2021](#)). The eccentricity and argument of periastron were parameterised using $\sqrt{e_p} \cos(\omega_p)$ and $\sqrt{e_p} \sin(\omega_p)$ for enhanced efficiency. Informative Gaussian priors were chosen for stellar mass and radius as well as the quadratic limb darkening coefficients of TESS. For the latter, we fitted a Gaussian to the coefficient estimates from Atlas and PHOENIX provided by [Claret \(2017\)](#), such that all coefficients with $T_{\text{eff}} \in [4000, 4500]$, $[\text{Fe}/\text{H}] \in [0, 0.2]$, $\log g \in [0, 0.2]$ lie

in the $R(f_{5\%})$ region of highest density of the prior, defined as $R(f_{\alpha}) = \{x : \mathbb{P}[x] > f_{\alpha}\}$ such that $P[x \in R(f_{\alpha})] = 1 - \alpha$. The quadratic limb darkening coefficients for the filters of the ground-based telescopes were sampled uniformly according to the sampling scheme of [Kipping \(2013\)](#). Weakly informative Gaussian priors were chosen for the transit times. Gaussian processes were used to model the stellar variability and instrumental trends in the TESS data. We also included a photometric jitter term for each ground-based observation and each TESS sector, which was added in quadrature to the respective flux uncertainties. Each of these jitter terms was sampled from a log-normal distribution, with a mean given by the standard deviation of the out-of-transit flux of the respective observation and a standard deviation of two.

The two different outlier removal strategies had little effect on the transit times inferred from the TESS data, but resulted in slight discrepancies between the posterior transit times of ground-based telescopes for three transits of planet b and one transit of planet c. In these cases, the posterior means of the two models were separated by more than one standard deviation of either distribution, resulting in differences up to 5.12 minutes for planet b and 1.3 minutes for planet c. We, thus, find that, at least in these cases, our posterior uncertainties underestimate the uncertainties that would arise if one were to marginalise across different strategies to remove outliers. Although marginalising over different outlier removal strategies would be desirable, it is computationally too expensive. Accordingly, we decided to use the mean and standard deviation of the stricter outlier removal strategy, that is the strategy in which more points were rejected as outliers, given that its the posterior transit time distributions had larger standard deviations in the discrepant cases.

4.2. Transit modelling and transit timing variations

We used a two-step approach to determine the initial parameters for the photo-dynamical analysis of the following Section 4.3. Firstly, we analysed, simultaneously, pre-detrended CHEOPS photometry, portioned TESS light curves, and new ASTEP+ photometry¹⁶ with PYORBIT ([Malavolta et al. 2016, 2018](#)). We used stellar parameters from Section 3 as Gaussian priors, and we computed quadratic limb-darkening (LD) with PYLDTK ([Husser et al. 2013](#); [Parviainen & Aigrain 2015](#)) for CHEOPS and TESS, while we decided to use Gaussian priors on quadratic LD coefficients $u_1 = 0.37 \pm 0.1$ and $u_2 = 0.25 \pm 0.1$ for ASTEP+, both B and R filters. We assumed fixed periods from previous incremental analysis (that is periods used to schedule CHEOPS visits) and circular orbits. We included CHEOPS V14 with PYCHEOPS-like detrending of $x - y$ offset as df/dx , d^2f/dx^2 , df/dy , d^2f/dy^2 , $d^2f/dxdy$, background (df/dbg), three harmonics of the satellite roll angle (ϕ) as $df/d \cos \phi$, $df/d \sin \phi$, $df/d \cos 2\phi$, $df/d \sin 2\phi$, $df/d \cos 3\phi$, $df/d \sin 3\phi$, a flux constant (f_{14}), and a linear term in time (df/dt). We detrended each ASTEP+ light curves for each filter taking into account a flux constant (f), a quadratic term (df/dt , d^2f/dt^2), the CCD position (df/dx , df/dy), FWHM value ($df/dfwhm$), and sky background ($df/dsky$). The transits have been modelled with the BATMAN package ([Kreidberg 2015](#)), and for the TESS Sector 13 we used a super-sampling factor of 30. The planetary and transit parameters of each planet have been shared across all the light curves, filters, and telescopes. We let free all the transit times (T_0 s) for each transit light curve.

¹⁶ These transits have been observed after last TESS sector and after the analysis of the older ground-based observations, so we decided to analyse them with the photo-dynamical approach.

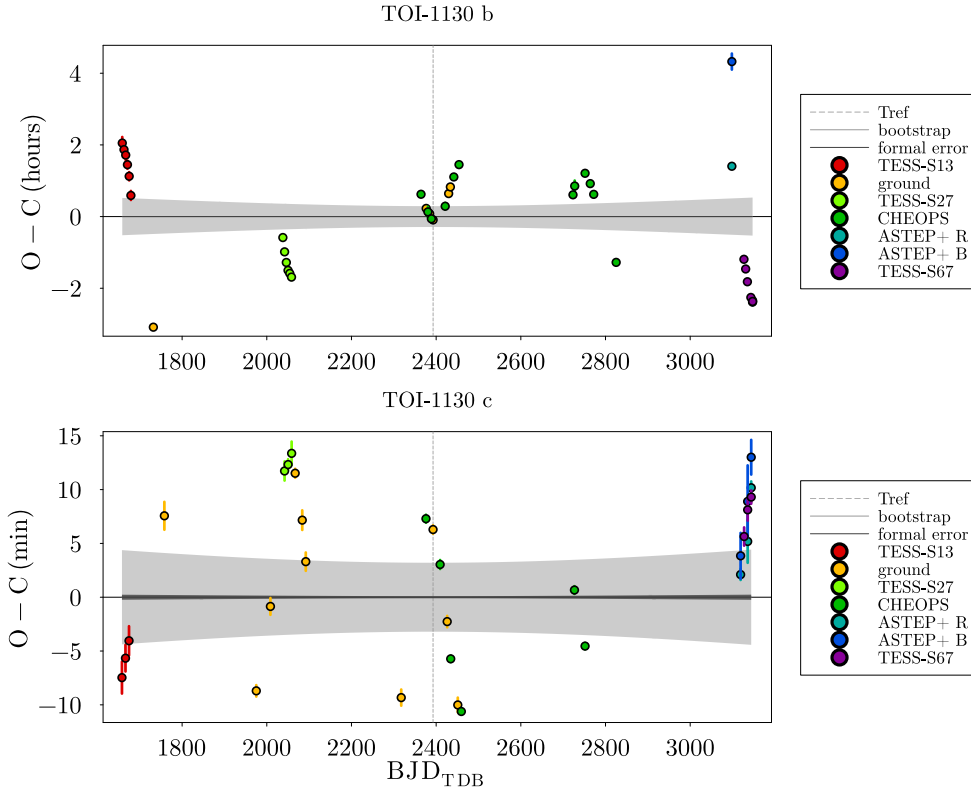


Fig. 1. Observed minus calculated (O-C) diagram of TOI-1130 b (top) and TOI-1130 c (bottom). The calculated T_{0S} were determined from the linear ephemeris: $T_{\text{lin},b,N} = 2392.81470 \pm 0.00021 (0.01260) + N \times 4.078668 \pm 0.000002 (0.000097) \text{BJD}_{\text{TDB}}$, and $T_{\text{lin},c,N} = 2392.66995 \pm 0.00007 (0.00218) + N \times 8.349560 \pm 0.000002 (0.000023) \text{BJD}_{\text{TDB}}$, with formal (thin-black area) and bootstrap (between round brackets, grey area) uncertainty. Ground-based T_{0S} presented in Sect. 2.1.3 and analysed in Sect. 4.1 are reported as ground. T_{ref} is the reference time of the linear ephemeris plotted as dashed-grey vertical line. All the times are in BJD, that is $\text{BJD}_{\text{TDB}} - 2457000$.

We decided to run PYORBIT combining the quasi-global optimiser PYDE (Storn & Price 1997; Parviainen et al. 2016) with a population¹⁷ of 328 for 50 000 generations and the EMCEE package (Foreman-Mackey et al. 2013, 2019) with 328 walkers for 2 000 000 steps. We removed the first 1 200 000 steps as burn-in, after checking the convergence of the chains by the Gelman-Rubin (Gelman & Rubin 1992) $\hat{R} < 1.01$ and the auto-correlation function (Foreman-Mackey et al. 2019), and we applied a thinning factor of 1 000 to reduce CPU and memory load. We take as best-fit parameters the maximum a posteriori (MAP) set, and we extract the T_{0S} (see Table A.2 and A.3) of each light curve and planet. We fitted new linear ephemeris (see Table A.2 and A.3 for planet b and c, respectively) and we created the observed minus calculated (O – C) diagrams (see Fig. 1) to assess the TTV signals.

Then, we run a dynamical analysis with TRADES¹⁸ (Borsato et al. 2014, 2019, 2021) using as observable the T_{0S} and the boundaries for some parameters from the PYORBIT analysis. We let run TRADES with PYDE with a population of 96 parameter set for 90 000 generations. Differently from previous analysis, we let vary also the eccentricities, e (and associated argument of pericenter, ω), and held fix the radii and the inclination of the planets. Fitting parameters (e.g. $\sqrt{e} \cos \omega$ and $\sqrt{e} \sin \omega$), boundaries, and priors were defined as in Nascimbeni et al. (2023). At the end of the analysis we extracted the best-fit solution and computed the masses and physical parameters, that we used, jointly with PYORBIT results, as initial parameters for the successive photo-dynamical approach.

4.3. Photo-dynamical modelling

The photo-dynamical approach allows us to simultaneously fit the transit photometry (with detrending), transit times, and radial velocities, during the dynamical integration of the full system. An upgraded version of TRADES (PHOTOTRADES) models transits with the PYTRANSIT package¹⁹ (Parviainen 2015). The code integrates the orbits of the planets and computes all the possible transit times with associated Keplerian elements. Then, it automatically (and blindly) selects the transit times and orbital elements of all the planets for each photometric portions, allowing us to model more planets for the same light curve portions, and pass them to PYTRANSIT. It does not take for planet-planet (mutual) occultation into account. However, to reduce the computational time and the number of parameters, we decided to use the photometry (with detrending when needed) as in the PYORBIT analysis (see Sect. 4.2), and only the T_{0S} for the transit from ground-based facilities analysed in Sect. 4.1. For each radial velocity data set we included an offset (γ) and jitter term (in \log_2), and a common linear trend in time (as in Korth et al. 2023) to take into account the possible influence of an additional planet on far outer orbit. To see all 116 fitted parameters with boundaries and priors in Table A.4.

We ran PHOTOTRADES with EMCEE with 232 walkers for 2 000 000 steps with a thinning factor of 100. We discarded the first 696 000 steps as burn-in after checking the convergence of the chains through visual inspection and with Gelman-Rubin (\hat{R}), Geweke (Geweke 1991), and ACF statistics. As representative of the best-fit solution we took the maximum a posteriori (MAP), the parameter set that maximise the log-probability. Due to the high complexity of the problem, some MAP parameters (fitted or physical) are outside of the 1σ uncertainty defined as the high density interval (HDI) at the 68.27%. In this case, we computed

¹⁷ In a Differential-Evolution optimiser the population is the number of configurations set (or orbital configurations) for each iteration (or generation). The population evolves with each iteration until the stopping criterion is reached.

¹⁸ <https://github.com/lucaborsato/trades>

¹⁹ <https://github.com/hpparvi/PyTransit>

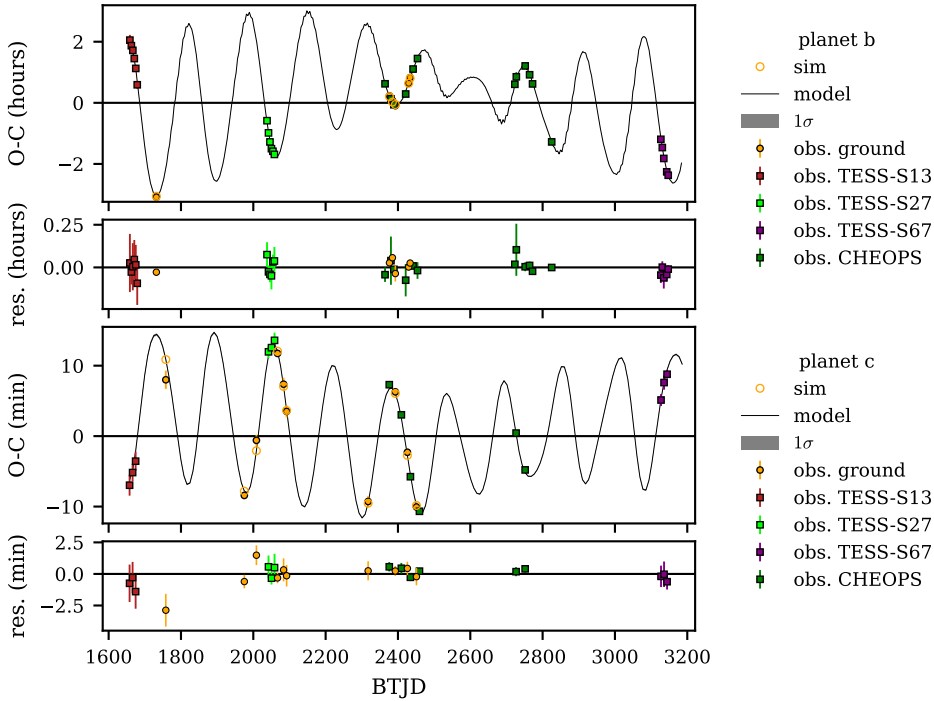


Fig. 2. Observed minus calculated ($O - C$) diagram of TOI-1130 b (top) and TOI-1130 c (bottom) from the photo-dynamical fit with TRADES of the ground-based T_{0s} (orange and black circles, with the simulated ones being as open orange circles) of photometry described in Sect. 4.1. The $O - C$ has been computed with the linear ephemeris in Tables A.2 and A.3. Observed transit times of TESS and CHEOPS, not used in the fit, have been over-plotted (as colour-coded squares) on the $O - C$ and residual panels, full MAP model as black line with 1σ grey-shaded area, that is almost invisible because the model is very well constrained. Times in BTJD = $\text{BJD}_{\text{TDB}} - 2\,457\,000$.

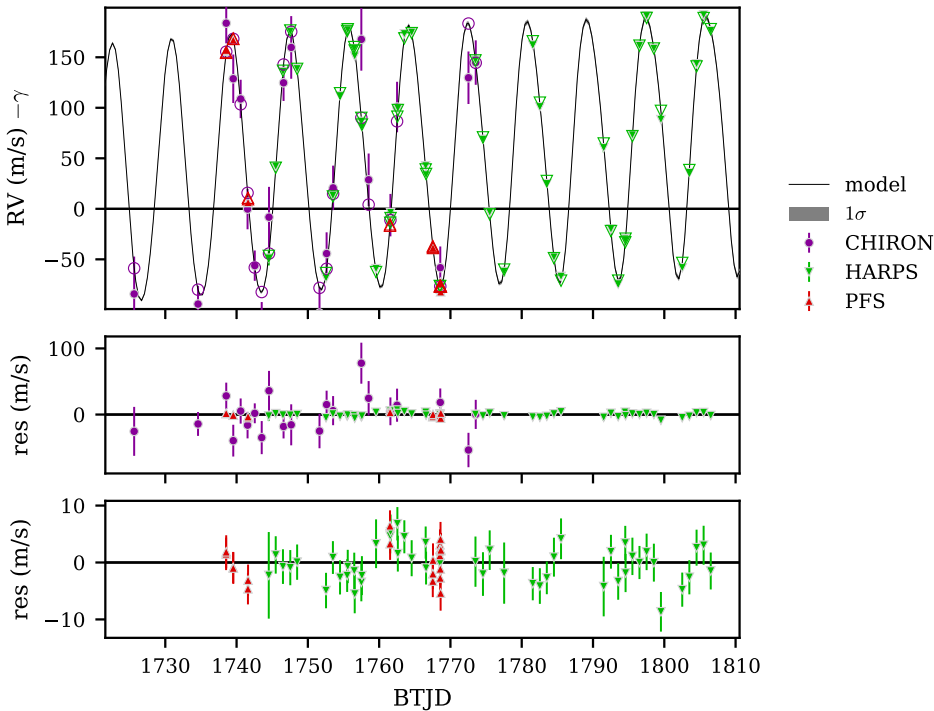


Fig. 3. Radial velocity (subtracted RV offset, γ) plot in the *top panel* with a different marker and colour for each data set. Observations as filled-markers and corresponding simulations as open-markers; full MAP model as black line with 1σ grey-shaded area. Residuals in *mid-panel* with all data sets. Residuals without the CHIRON data set in the *bottom-panel*. Times in BTJD = $\text{BJD}_{\text{TDB}} - 2\,457\,000$.

and reported the HDI at the 95.44% as 2σ equivalent. See the full report of the fitted and physical parameters in Table A.4. See $O - C$ diagram of the ground-based T_{0s} in Fig. 2, RV plot in Fig. 3, and photometry in Fig. A.1 (with photometric residuals in Fig. A.2).

We searched for additional signals in the Doppler data computing the generalised Lomb-Scargle²⁰ periodogram (GLS, Zechmeister & Kürster 2009) of the HARPS and PFS RV residuals. We found no significant signals in the power spectrum, with the highest peak in the GLS periodogram having a relatively high

false alarm probability (FAP) of $\sim 10\%$, as derived using a bootstrap randomisation approach with 10 000 repetitions (Hatzes 2019).

5. Discussions

5.1. Mean-motion resonance analysis

For a pair of planets close enough to a first order mean-motion resonance (MMR), the expected TTVs is made of two terms: the evolution of the resonant angle (ϕ), whose period is roughly proportional to $(m/m_\star)^{-2/3} P_{\text{orb}}$, where m is comparable to the mass of the planets, and a slower term linked to the evolution of the

²⁰ Implemented in JULIA version available at <http://juliaastro.org/LombScargle.jl/stable/>

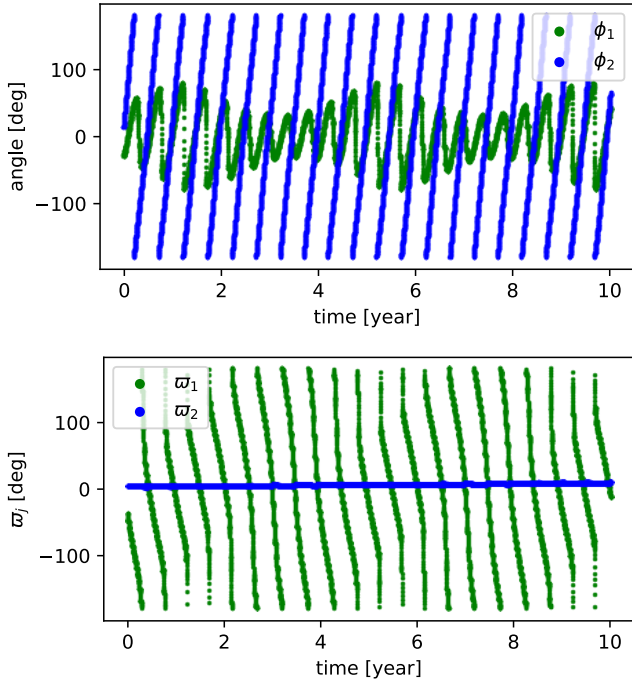


Fig. 4. Example of evolution of the angles for a sample of the posterior. The top panel shows the resonant angles $\phi_1 = \lambda_1 - 2\lambda_2 + \varpi_1$ and $\phi_2 = \lambda_1 - 2\lambda_2 + \varpi_2$, where 1 refers to planet b and 2 to planet c, λ is the mean longitude and ϖ the longitude of periastron of the planets. The bottom panel shows the evolution of the longitude of periastron.

eccentricities and longitude of periastron (Nesvorný & Vokrouhlický 2016). The relation between these two periods depend on the position of the system with respect to the exact resonance. Often, and in particular for smaller planets, an observation baseline of a few years only allow to observe the effect of the resonant angle, resulting in a mostly sinusoidal TTV signal. However, in the case of TOI-1130, the period of the two terms appear to be very close, with the period of precession of the inner orbit only slightly slower than the evolution of the resonant angle ϕ_1 , see Fig. 4. Adding up these two terms with similar period results in a TTV signal that appears to be modulated in amplitude, see Fig. 2.

The good constraints that we get for the resonant term of the TTVs allows us to constrain the resonant part of the architecture, as can be seen in Fig. 5. In that figure, we can see that the system lies outside the formal resonant domain (red area in the figure), unlike, for example, TOI-216 (Nesvorný et al. 2022). Observing the resonant term on its own does not allow to constrain the non-resonant part of the eccentricities, often resulting in a highly degenerated posterior for the eccentricities and longitudes of periastron (Leleu et al. 2021b, 2022, 2023). However, for TOI-1130, we can see the effect of the evolution of the periastron and the eccentricities on the TTVs, resulting in good constraints on these parameters.

Assuming that the pair was initially captured into the 2:1 due to a convergent migration in the proto-planetary disk (e.g. Weidenschilling & Davis 1985; Terquem & Papaloizou 2007), the observed architecture of the system enables in-depth study of its long term tidal evolution. Indeed, for planets whose orbital period is typically below 10 days, tides are expected to be an efficient mechanism to damp the eccentricity of the planet, effectively pushing the planets outside of the exact resonance (e.g. Novak et al. 2003; Lee et al. 2013; Delisle & Laskar 2014).

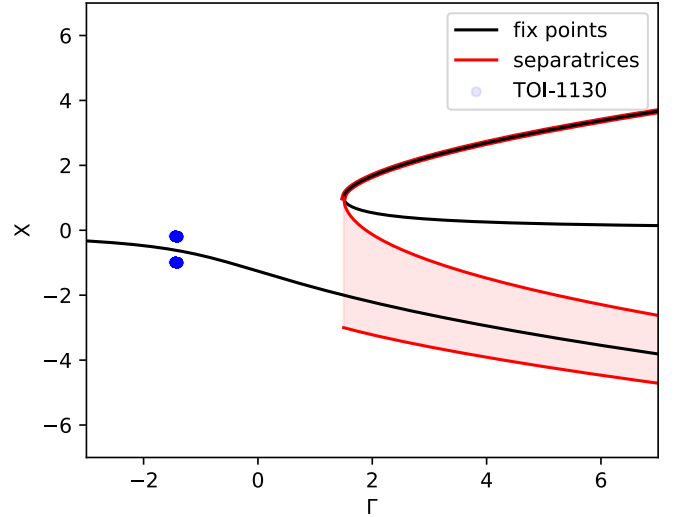


Fig. 5. 1-degree of freedom model of the 2:1 MMR (Henrard & Lemaître 1983; Deck et al. 2013). We note that X and Γ are function of the orbital elements and masses of the system. Γ represent how deep the system is in the resonance, while X parameterise the position of the fix points and separatrices. The blue dots represent the intersection of 300 randomly-selected samples of the posterior with the X - Γ plane.

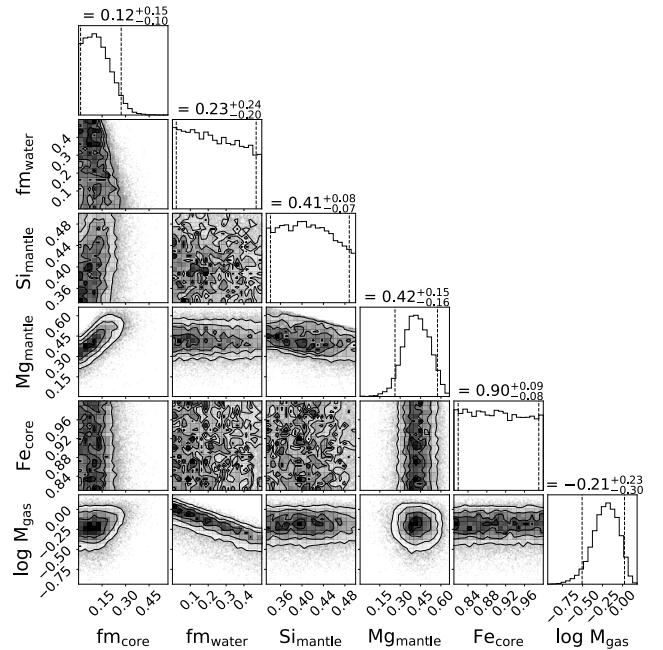


Fig. 6. Inferred interior structure parameters of TOI-1130 b, with the values and errors above each histogram corresponding to the median and 5th and 95th percentile of each posterior distribution. The shown parameters are the mass fractions of the inner core and water layer (with respect to the solid part of the planet, they add up to 1 together with the mantle mass fraction), the elemental molar fractions of Si and Mg in the mantle and Fe in the inner core and the logarithm of the total H/He mass in Earth masses.

5.2. Internal structure modelling

We modelled the interior structure of TOI-1130 b using a Bayesian inference scheme, following the method introduced in Leleu et al. (2021a), which is based on Dorn et al. (2017). The forward model used is an early version of Haldemann et al. (2024) and uses equations of state from Hakim et al. (2018), Sotin et al. (2007) and Haldemann et al. (2020) to model each

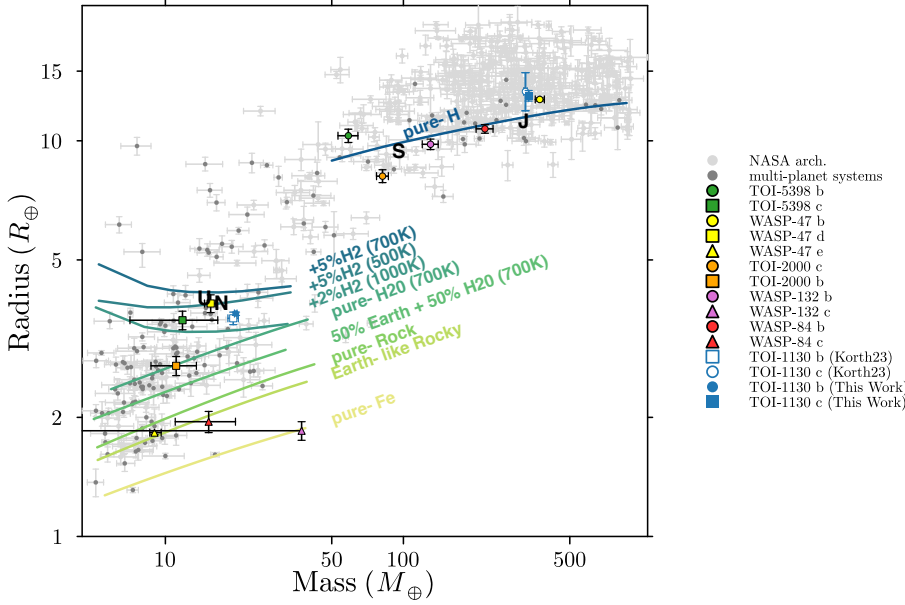


Fig. 7. Mass-radius relation plot with data from the NASA Exoplanet archive for exoplanets with a mass and radius precision lower than 20%. Models (plotted as colour-coded lines) from Zeng et al. (2019) and <https://lweb.cfa.harvard.edu/~lzeng/planetmodels.html#rrrelation>. We plotted TOI-1130 b as square, white-fill blue-stroke from Korth et al. (2023) and full-blue from this work; TOI-1130 c as circle, same colour-code of TOI-1130 b. Over-plotted as dark-grey circles the multi-planet systems and a sample of TOI-1130-like systems with different colours (based on host-name and with black outer stroke) and markers (based on planet type, circle for giants, triangle for $R_p \leq 2 R_\oplus$, and square in between): TOI-5398 (Mantovan et al. 2024), WASP-47 (Nascimbeni et al. 2023), TOI-2000 (Sha et al. 2023), WASP-132 (Hellier et al. 2017; Hord et al. 2022), and WASP-84 (Maciejewski et al. 2023). Over-plotted, also, Neptune (N), Uranus (U), Saturn (S), and Jupiter (J).

planet as a spherically symmetric structure made up of an inner iron core with up to 19% of sulphur, a silicate mantle made up of oxidised Si, Mg, and Fe and a condensed water layer. On top of each such structure, a H/He envelope is modelled separately following Lopez & Fortney (2014). The elemental Si/Mg/Fe ratios are assumed to be stellar, following Thiabaud et al. (2015). While other studies find that at least for rocky planets this correlation might not be 1:1 (Adibekyan et al. 2021), the low density of TOI-1130 b, which means that it likely hosts a thick atmosphere, renders this assumption more reliable.

For the Bayesian inference, we use a uniform prior for the mass fractions of the inner core, mantle and water layer (on the simplex on which they add up to 1), with an upper limit of 0.5 for the water mass fraction (Thiabaud et al. 2014; Marboeuf et al. 2014). The mass of the H/He layer is sampled from a log-uniform prior. As the problem of modelling the internal structure of a planet is highly degenerate, the results of our analysis do depend to a certain extent on the chosen priors.

The resulting constraints on the internal structure of TOI-1130 b are summarised in Figure 6. According to our model, the planet hosts a H/He envelope with a mass of $M_{\text{gas}} = 0.62^{+0.43}_{-0.31} M_\oplus$ and a thickness of $R_{\text{gas}} = 1.26^{+0.27}_{-0.25} R_\oplus$, where the values and errors correspond to the median and 5th and 95th percentiles of the posterior distributions. The presence and mass of a potential water layer remains fully unconstrained. However, these results are affected by our model only considering water in condensed form and modelling the H/He envelope independently from the rest of the planet, thereby neglecting any pressure and temperature effects it has on the rest of the planet.

6. Conclusions

In this work we improved our knowledge on the multi-planet system TOI-1130 by re-analysing the whole transits and radial velocities presented in Korth et al. (2023) and with an additional TESS sector, six ground-based ASTEP+ transits, and 17 new high-precision photometric data observed with the CHEOPS satellite.

From the full photo-dynamical model with TRADES we obtained stellar parameters, R_\star , ρ_\star , and M_\star , within 1σ of our priors, but only R_\star is consistent with the value derived by

Korth et al. (2023). This could be due to (1) different priors used (parameters determined with different methods and codes), (2) different parameterisation (we fitted R_\star and ρ_\star instead of R_\star and M_\star), (3) and longer baseline (~ 2 yr) of additional photometric data with very-high precision CHEOPS light curves.

We found that $M_b = 19.8^{+0.2}_{-0.3} M_\oplus$, both radii ($R_b = 3.66^{+0.03}_{-0.04} R_\oplus$, $R_c = 13.0^{+0.4}_{-0.4} R_\oplus$) and densities ($\rho_b = 0.41^{+0.01}_{-0.01} \rho_\oplus$, $\rho_c = 0.15^{+0.01}_{-0.02} \rho_\oplus$) agree with Korth et al. (2023) within 1σ , while $M_c = 336^{+2}_{-5} M_\oplus$ is consistent only at 2σ . Thanks to CHEOPS light curves with very high photometric precision, and with additional ASTEP+ data, the determined precision of each parameter is higher than Korth et al. (2023), in particular $\sigma_{M_b} \lesssim 1.5\%$, $\sigma_{R_b} \lesssim 1.1\%$, $\sigma_{M_c} \lesssim 1.5\%$, $\sigma_{R_c} \lesssim 3\%$. Those values imply a precision of $\sim 3\%$ and $\sim 11\%$ on the densities of planet b and c, respectively. A comparison with Korth et al. (2023) values and other similar systems can be seen in the mass-radius relation in Fig. 7. We fitted eccentricities with flat-uniform priors in $(\sqrt{e} \cos \omega, \sqrt{e} \sin \omega)$ form and we also found that both planets have slightly eccentric orbits as suggested by Korth et al. (2023), but e_b is consistent within 2σ , while we found a lower e_c consistent with their value only at 4σ .

Although we were unable to fit for an additional outer planet due to the current data, we were able to tentatively estimate the minimum mass ($M_d \sin i$) and semi-major axis (a_d) of candidate planet d from the linear trend in the radial velocities. The period P_d was assumed to be 161.762 days, which is twice the total time spanned by the RV observations. Asymmetric Gaussian was generated for the stellar mass (M_\star) and RV linear trend from the photo-dynamical posterior. The expected linear RVs were computed for each generated RV linear trend, and the semi-amplitude K_{RV} was estimated as the difference between the maximum and minimum values. Inverting the equation $K_{\text{RV}} \approx (M_d \sin i) n a / M_\star$, with the mean motion $n = 2\pi/P_d$, and $a^3 = GM_\star/n^2$, we found $a_d = 0.527 \pm 0.002$ au and $M_d \sin i = 0.866^{+0.025}_{-0.032} M_{\text{Jup}}$. However, these values strongly depend on the assumption that the period of this candidate is approximately twice the time elapsed during RV observations. Observing only a linear trend in the RV, it is possible that the period is longer, resulting in a higher mass. The GLS analysis of RV residuals of PFS and HARPS does not exhibit a significant signal (FAP $\sim 10\%$). Further radial velocity measurements would

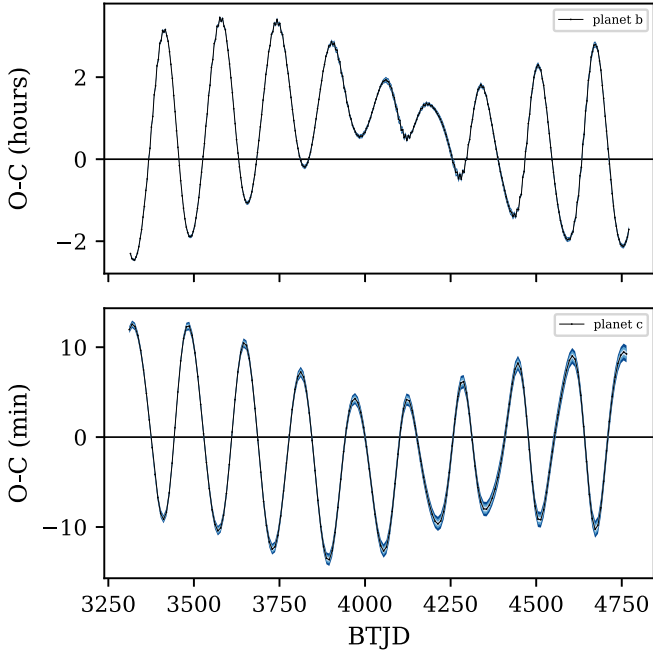


Fig. 8. O-C diagram of the synthetic T_0 s predicted with the MAP orbital solution (black dots are connected by a black line) from the photo-TRADES analysis. Uncertainty plotted as 3σ in dark-blue, 2σ in light-blue, and 1σ whitish-blue. The x -axis in BTJD = BJD_{TDB} – 2 457 000 ranges from 2024 until 2028.

increase the temporal baseline needed to detect the correct period of the outer candidate.

The lower relative errors we obtained in the orbital parameters allows us to predict the future transit times (see the O-C diagram in Fig. 8), until 2028²¹, with a very high precision ($\sigma_{T_0, \max} = 2.6$ min and 20 s for planet b and c, respectively). This is very important because the precise knowledge of when both planets transit is of fundamental importance for the upcoming transmission spectroscopy observations with JWST (Gardner et al. 2023) and Ariel (Tinetti et al. 2018). In fact, TOI-1130 c is one of the planets with the highest Transmission Spectroscopic Metric (TSM, Kempton et al. 2018), and both planets are part of a JWST proposal²². JWST and Ariel observations will allow us to characterise atmospheric abundances which are, as suggested by Korth et al. (2023), crucial to understand the formation process that the system underwent.

Data availability

Photometry of TESS, CHEOPS, and ASTEP+, and transit times prediction are available at the CDS via anonymous ftp to cdsarc.cds.unistra.fr (130.79.128.5) or via <https://cdsarc.cds.unistra.fr/viz-bin/cat/J/A+A/689/A52>. Data type: Observed-Fitted transit times in ascii file; ASTEP+ and CHEOPS-PIPE data and best-fit model in ascii file; predicted transit times from 2024 to 2028 in ascii file.

Acknowledgements. CHEOPS is an ESA mission in partnership with Switzerland with important contributions to the payload and the ground segment from Austria, Belgium, France, Germany, Hungary, Italy, Portugal, Spain, Sweden, and the United Kingdom. The CHEOPS Consortium would like to gratefully acknowledge the support received by all the agencies, offices, universities, and industries involved. Their flexibility and willingness to explore new approaches

²¹ We will provide the predicted transits with uncertainties as electronic form through CDS.

²² JWST Proposal GO 3385, P.I. Chelsea Huang (Huang et al. 2023).

were essential to the success of this mission. CHEOPS data analysed in this article will be made available in the CHEOPS mission archive (https://cheops.unige.ch/archive_browser/). LBo, GBr, VN, IPa, GPI, RRA, GSc, VSi, and TZi acknowledge support from CHEOPS ASI-INAF agreement no. 2019-29-HH.0. This work has been carried out within the framework of the NCCR PlanetS supported by the Swiss National Science Foundation under grants 51NF40_182901 and 51NF40_205606. AL acknowledges support of the Swiss National Science Foundation under grant number TMSG12_211697. This work has been carried out within the framework of the NCCR PlanetS supported by the Swiss National Science Foundation under grants 51NF40_182901 and 51NF40_205606. This work uses data obtained with the ASTEP+ telescope, at Concordia Station in Antarctica. ASTEP+ benefited from the support of the French and Italian polar agencies IPEV and PNRA in the framework of the Concordia station program, from OCA, INSU, Idex UCAJEDI (ANR-15-IDEX-01) and ESA through the Science Faculty of the European Space Research and Technology Centre (ESTEC). The Birmingham contribution to ASTEP+ is supported by the European Union’s Horizon 2020 research and innovation programme (grant’s agreement no. 803193/BEBOP), and from the Science and Technology Facilities Council (STFC; grant no. ST/S00193X/1, and ST/W002582/1). ABr was supported by the SNSA. ACC acknowledges support from STFC consolidated grant number ST/V000861/1, and UKSA grant number ST/X002217/1. MNG is the ESA CHEOPS Project Scientist and Mission Representative, and as such also responsible for the Guest Observers (GO) Programme. MNG does not relay proprietary information between the GO and Guaranteed Time Observation (GTO) Programmes, and does not decide on the definition and target selection of the GTO Programme. TWi acknowledges support from the UKSA and the University of Warwick. TZi acknowledges NVIDIA Academic Hardware Grant Program for the use of the Titan V GPU card and the Italian MUR Departments of Excellence grant 2023–2027 “Quantum Frontiers”. DG gratefully acknowledges the financial support from the grant for internationalization (GAND_GFI_23_01) provided by the University of Turin (Italy). YAI acknowledges support from the Swiss National Science Foundation (SNSF) under grant 200020_192038. We acknowledge financial support from the Agencia Estatal de Investigación of the Ministerio de Ciencia e Innovación MCIN/AEI/10.13039/501100011033 and the ERDF “A way of making Europe” through projects PID2019-107061GB-C61, PID2019-107061GB-C66, PID2021-125627OB-C31, and PID2021-125627OB-C32, from the Centre of Excellence “Severo Ochoa” award to the Instituto de Astrofísica de Canarias (CEX2019-000920-S), from the Centre of Excellence “María de Maeztu” award to the Institut de Ciències de l’Espai (CEX2020-001058-M), and from the Generalitat de Catalunya/CERCA programme. We acknowledge financial support from the Agencia Estatal de Investigación of the Ministerio de Ciencia e Innovación MCIN/AEI/10.13039/501100011033 and the ERDF “A way of making Europe” through projects PID2019-107061GB-C61, PID2019-107061GB-C66, PID2021-125627OB-C31, and PID2021-125627OB-C32, from the Centre of Excellence “Severo Ochoa” award to the Instituto de Astrofísica de Canarias (CEX2019-000920-S), from the Centre of Excellence “María de Maeztu” award to the Institut de Ciències de l’Espai (CEX2020-001058-M), and from the Generalitat de Catalunya/CERCA programme. S.C.C.B. acknowledges support from FCT through FCT contracts nr. IF/01312/2014/CP1215/CT0004. C.B. acknowledges support from the Swiss Space Office through the ESA PRODEX program. P.E.C. is funded by the Austrian Science Fund (FWF) Erwin Schrodinger Fellowship, program J4595-N. This project was supported by the CNES. The Belgian participation to CHEOPS has been supported by the Belgian Federal Science Policy Office (BELSPO) in the framework of the PRODEX Program, and by the University of Liège through an ARC grant for Concerted Research Actions financed by the Wallonia-Brussels Federation. L.D. thanks the Belgian Federal Science Policy Office (BELSPO) for the provision of financial support in the framework of the PRODEX Programme of the European Space Agency (ESA) under contract number 4000142531. This work was supported by FCT - Fundação para a Ciência e a Tecnologia through national funds and by FEDER through COMPETE2020 through the research grants UIDB/04434/2020, UIDP/04434/2020, 2022.06962.PTDC. O.D.S.D. is supported in the form of work contract (DL 57/2016/CP1364/CT0004) funded by national funds through FCT. B.-O. D. acknowledges support from the Swiss State Secretariat for Education, Research and Innovation (SERI) under contract number MB22.00046. This project has received funding from the Swiss National Science Foundation for project 200021_200726. It has also been carried out within the framework of the National Centre of Competence in Research PlanetS supported by the Swiss National Science Foundation under grant 51NF40_205606. The authors acknowledge the financial support of the SNSF. MF and CMP gratefully acknowledge the support of the Swedish National Space Agency (DNR 65/19, 174/18). M.G. is an F.R.S.-FNRS Senior Research Associate. CHE acknowledges support from the European Union H2020-MSCA-ITN-2019 under Grant Agreement no. 860470 (CHAMELEON). SH gratefully acknowledges CNES funding through the grant 837319. KGI is the ESA CHEOPS Project Scientist and is responsible for the ESA CHEOPS Guest Observers Programme. She does not participate in, or contribute to, the definition of the Guaranteed Time Programme

of the CHEOPS mission through which observations described in this paper have been taken, nor to any aspect of target selection for the programme. J.K. acknowledges the Swedish Research Council (VR: Etableringsbidrag 2017-04945), and the common acknowledgment A.C., A.D., B.E., K.G., and J.K. acknowledge their role as ESA-appointed CHEOPS Science Team Members. K.W.F.L. was supported by Deutsche Forschungsgemeinschaft grants RA714/14-1 within the DFG Schwerpunkt SPP 1992, Exploring the Diversity of Extrasolar Planets. This work was granted access to the HPC resources of MesoPSL financed by the Region Ile de France and the project Equip@Meso (reference ANR-10-EQPX-29-01) of the programme Investissements d’Avenir supervised by the Agence Nationale pour la Recherche. M.L. acknowledges support of the Swiss National Science Foundation under grant number PCEFP2_194576. P.M. acknowledges support from STFC research grant number ST/R000638/1. This work was also partially supported by a grant from the Simons Foundation (PI Queloz, grant number 327127). NCSa acknowledges funding by the European Union (ERC, FIERCE, 101052347). Views and opinions expressed are however those of the author(s) only and do not necessarily reflect those of the European Union or the European Research Council. Neither the European Union nor the granting authority can be held responsible for them. A.S. acknowledges support from the Swiss Space Office through the ESA PRODEX program. S.G.S. acknowledge support from FCT through FCT contract nr. CEECIND/00826/2018 and POPH/FSE (EC). The Portuguese team thanks the Portuguese Space Agency for the provision of financial support in the framework of the PRODEX Programme of the European Space Agency (ESA) under contract number 4000142255. GyMSz acknowledges the support of the Hungarian National Research, Development and Innovation Office (NKFIH) grant K-125015, a PRODEX Experiment Agreement No. 4000137122, the Lendület LP2018-7/2021 grant of the Hungarian Academy of Science and the support of the city of Szombathely. V.V.G. is an F.R.S-FNRS Research Associate. J.V. acknowledges support from the Swiss National Science Foundation (SNSF) under grant PZ00P2_208945. N.A.W. acknowledges UKSA grant ST/R004838/1. A.H.M.J.T. acknowledges receiving funding from the Science and Technology Facilities Council (STFC; grant n° ST/S00193X/1). A.C.M.C. acknowledges support from the FCT, Portugal, through the CFisUC projects UIDB/04564/2020 and UIDP/04564/2020, with DOI identifiers 10.54499/UIDB/04564/2020 and 10.54499/UIDP/04564/2020, respectively.

Software. The following software and packages have been used in this work: NUMPY (Harris et al. 2020), MATPLOTLIB (Hunter 2007), SCIPY (Virtanen et al. 2020), H5PY, and JULIA²³ (Bezanson et al. 2017).

References

- Adibekyan, V., Dorn, C., Sousa, S. G., et al. 2021, *Science*, 374, 330
- Agol, E., Steffen, J., Sari, R., & Clarkson, W. 2005, *MNRAS*, 359, 567
- Agol, E., Luger, R., & Foreman-Mackey, D. 2020, *AJ*, 159, 123
- Astropy Collaboration (Robitaille, T. P., et al.) 2013, *A&A*, 558, A33
- Astropy Collaboration (Price-Whelan, A. M. et al.) 2018, *AJ*, 156, 123
- Barnes, S. A. 2010, *ApJ*, 722, 222
- Baruteau, C., Bai, X., Mordasini, C., & Mollière, P. 2016, *Space Sci. Rev.*, 205, 77
- Becker, J. C., Vanderburg, A., Adams, F. C., Rappaport, S. A., & Schwengeler, H. M. 2015, *ApJ*, 812, L18
- Benz, W., Broeg, C., Fortier, A., et al. 2021, *Ex. Astron.*, 51, 109
- Bezanson, J., Edelman, A., Karpinski, S., & Shah, V. B. 2017, *SIAM Rev.*, 59, 65
- Blackwell, D. E., & Shallis, M. J. 1977, *MNRAS*, 180, 177
- Bonfanti, A., Ortolani, S., Piotto, G., & Nascimbeni, V. 2015, *A&A*, 575, A18
- Bonfanti, A., Ortolani, S., & Nascimbeni, V. 2016, *A&A*, 585, A5
- Bonfanti, A., Delrez, L., Hooton, M. J., et al. 2021, *A&A*, 646, A157
- Borsato, L., Marzari, F., Nascimbeni, V., et al. 2014, *A&A*, 571, A38
- Borsato, L., Malavolta, L., Piotto, G., et al. 2019, *MNRAS*, 484, 3233
- Borsato, L., Piotto, G., Gandolfi, D., et al. 2021, *MNRAS*, 506, 3810
- Brandeker, A., Heng, K., Lendl, M., et al. 2022, *A&A*, 659, A4
- Bryant, E. M., & Bayliss, D. 2022, *AJ*, 163, 197
- Cañas, C. I., Wang, S., Mahadevan, S., et al. 2019, *ApJ*, 870, L17
- Castelli, F., & Kurucz, R. L. 2003, in *IAU Symp.*, 210, Modelling of Stellar Atmospheres, eds. N. Piskunov, W. W. Weiss, & D. F. Gray, A20
- Chatterjee, S., Ford, E. B., Matsumura, S., & Rasio, F. A. 2008, *ApJ*, 686, 580
- Claret, A. 2017, *A&A*, 600, A30
- Crane, J. D., Shectman, S. A., & Butler, R. P. 2006, *SPIE Conf. Ser.*, 6269, 62693J
- Crane, J. D., Shectman, S. A., Butler, R. P., Thompson, I. B., & Burley, G. S. 2008, *SPIE Conf. Ser.*, 7014, 701479
- Crane, J. D., Shectman, S. A., Butler, R. P., et al. 2010, *SPIE Conf. Ser.*, 7735, 773553
- Deck, K. M., Payne, M., & Holman, M. J. 2013, *ApJ*, 774, 129
- Degen, D. 2022, Master’s thesis, Eidgenössische Technische Hochschule Zürich (ETHZ), Switzerland
- Delisle, J. B., & Laskar, J. 2014, *A&A*, 570, L7
- Dorn, C., Venturini, J., Khan, A., et al. 2017, *A&A*, 597, A37
- Foreman-Mackey, D., Hogg, D. W., Lang, D., & Goodman, J. 2013, *PASP*, 125, 306
- Foreman-Mackey, D., Farr, W., Sinha, M., et al. 2019, *J. Open Source Softw.*, 4, 1864
- Foreman-Mackey, D., Luger, R., Agol, E., et al. 2021a, *J. Open Source Softw.*, 6, 3285
- Foreman-Mackey, D., Savel, A., Luger, R., et al. 2021b, exoplanet-dev/exoplanet v0.5.1, <https://doi.org/10.5281/zenodo.1998447>
- Gaia Collaboration (Vallenari, A., et al.) 2023, *A&A*, 674, A1
- Gardner, J. P., Mather, J. C., Abbott, R., et al. 2023, *PASP*, 135, 068001
- Gelman, A., & Rubin, D. B. 1992, *Stat. Sci.*, 7, 457
- Geweke, J. F. 1991, *Evaluating the Accuracy of Sampling-based Approaches to the Calculation of Posterior Moments*, Staff Report 148, Federal Reserve Bank of Minneapolis
- Gray, D. F. 2008, *The Observation and Analysis of Stellar Photospheres* (Cambridge University Press)
- Guillot, T., Abe, L., Agabi, A., et al. 2015, *Astron. Nachr.*, 336, 638
- Gustafsson, B., Edvardsson, B., Eriksson, K., et al. 2008, *A&A*, 486, 951
- Hakim, K., Rivoldini, A., Van Hoolst, T., et al. 2018, *Icarus*, 313, 61
- Haldemann, J., Alibert, Y., Mordasini, C., & Benz, W. 2020, *A&A*, 643, A105
- Haldemann, J., Dorn, C., Venturini, J., Alibert, Y., & Benz, W. 2024, *A&A*, 681, A96
- Harris, C. R., Millman, K. J., van der Walt, S. J., et al. 2020, *Nature*, 585, 357–362
- Hatzes, A. P. 2019, *The Doppler Method for the Detection of Exoplanets* (IOP Publishing), 2514
- Hellier, C., Anderson, D. R., Collier Cameron, A., et al. 2012, *MNRAS*, 426, 739
- Hellier, C., Anderson, D. R., Collier Cameron, A., et al. 2017, *MNRAS*, 465, 3693
- Henrad, J., & Lemaître, A. 1983, *Celest. Mech.*, 30, 197
- Holman, M. J., & Murray, N. W. 2005, *Science*, 307, 1288
- Hord, B. J., Colón, K. D., Berger, T. A., et al. 2022, *AJ*, 164, 13
- Hoyer, S., Guterman, P., Demangeon, O., et al. 2020, *A&A*, 635, A24
- Huang, C. X., Wu, Y., & Triard, A. H. M. J. 2016, *ApJ*, 825, 98
- Huang, C. X., Quinn, S. N., Vanderburg, A., et al. 2020a, *ApJ*, 892, L7
- Huang, C. X., Vanderburg, A., Pál, A., et al. 2020b, *RNAAS*, 4, 204
- Huang, C. X., Vanderburg, A., Korth, J., et al. 2023, *The first comparative atmospheric study of a Jovian planet and a sub-Neptune in the TOI-1130 system*, JWST Proposal, Cycle 2, ID. #3385
- Hunter, J. D. 2007, *Comput. Sci. Eng.*, 9, 90
- Husser, T.-O., Wende-von Berg, S., Dreizler, S., et al. 2013, *A&A*, 553, A6
- Jackson, J. M., Dawson, R. I., Quarles, B., & Dong, J. 2023, *AJ*, 165, 82
- Jenkins, J. M., Twicken, J. D., McCauliff, S., et al. 2016, *SPIE Conf. Ser.*, 9913, 99133E
- Kempton, E. M. R., Bean, J. L., Louie, D. R., et al. 2018, *PASP*, 130, 114401
- Kipping, D. M. 2013, *MNRAS*, 435, 2152
- Kley, W. 2019, *Planet Formation and Disk–Planet Interactions*, eds. M. Audard, M. R. Meyer, & Y. Alibert (Berlin, Heidelberg: Springer Berlin Heidelberg), 151
- Korth, J., Gandolfi, D., Šubjak, J., et al. 2023, *A&A*, 675, A115
- Kreidberg, L. 2015, *PASP*, 127, 1161
- Kumar, R., Carroll, C., Hartikainen, A., & Martin, O. 2019, *J. Open Source Softw.*, 4, 1143
- Kurucz, R. L. 2013, ATLAS12: Opacity sampling model atmosphere program, Astrophysics Source Code Library [[record ascl:1303.024](https://ui.adsabs.org/abs/2013ASCL..1303..024K)]
- Latham, D. W., Rowe, J. F., Quinn, S. N., et al. 2011, *ApJ*, 732, L24
- Lee, M. H., Fabrycky, D., & Lin, D. N. C. 2013, *ApJ*, 774, 52
- Leleu, A., Alibert, Y., Hara, N. C., et al. 2021a, *A&A*, 649, A26
- Leleu, A., Chatel, G., Udry, S., et al. 2021b, *A&A*, 655, A66
- Leleu, A., Delisle, J. B., Mardling, R., et al. 2022, *A&A*, 661, A141
- Leleu, A., Delisle, J. B., Udry, S., et al. 2023, *A&A*, 669, A117
- Lin, D. N. C., Bodenheimer, P., & Richardson, D. C. 1996, *Nature*, 380, 606
- Lindgren, L., Bastian, U., Biermann, M., et al. 2021, *A&A*, 649, A4
- Lopez, E. D., & Fortney, J. J. 2014, *ApJ*, 792, 1
- Luger, R., Agol, E., Foreman-Mackey, D., et al. 2019, *AJ*, 157, 64
- Maciejewski, G., Golenka, J., Łoboda, W., et al. 2023, *MNRAS*, 525, L43
- Malavolta, L., Nascimbeni, V., Piotto, G., et al. 2016, *A&A*, 588, A118
- Malavolta, L., Mayo, A. W., Loudon, T., et al. 2018, *AJ*, 155, 107
- Mantovan, G., Montalto, M., Piotto, G., et al. 2022, *MNRAS*, 516, 4432

²³ <https://julialang.org/>

- Mantovan, G., Malavolta, L., Desidera, S., et al. 2024, *A&A*, **682**, A129
- Marboeuf, U., Thiabaud, A., Alibert, Y., Cabral, N., & Benz, W. 2014, *A&A*, **570**, A36
- Marigo, P., Girardi, L., Bressan, A., et al. 2017, *ApJ*, **835**, 77
- Maxted, P. F. L., Ehrenreich, D., Wilson, T. G., et al. 2022, *MNRAS*, **514**, 77
- Mayor, M., Pepe, F., Queloz, D., et al. 2003, *The Messenger*, **114**, 20
- Mékarnia, D., Guillot, T., Rivet, J. P., et al. 2016, *MNRAS*, **463**, 45
- Moré, J. J., Garbow, B. S., & Hillstrome, K. E. 1980, *User guide for MINPACK-1*, Tech. Rep. ANL-80-74, Argonne Nat. Lab., Argonne, IL
- Morris, B. M., Delrez, L., Brandeker, A., et al. 2021, *A&A*, **653**, A173
- Nagasawa, M., Ida, S., & Bessho, T. 2008, *ApJ*, **678**, 498
- Nascimbeni, V., Borsato, L., Zingales, T., et al. 2023, *A&A*, **673**, A42
- Nesvorný, D., & Vokrouhlický, D. 2016, *ApJ*, **823**, 72
- Nesvorný, D., Chrenko, O., & Flock, M. 2022, *ApJ*, **925**, 38
- Novak, G. S., Lai, D., & Lin, D. N. C. 2003, *Scientific Frontiers in Research on Extrasolar Planets*, eds. D. Deming, & S. Seager, *ASP Conf. Ser.*, **294**, 177
- Parviainen, H. 2015, *MNRAS*, **450**, 3233
- Parviainen, H., & Aigrain, S. 2015, *MNRAS*, **453**, 3821
- Parviainen, H., Pallé, E., Nortmann, L., et al. 2016, *A&A*, **585**, A114
- Persson, C. M., Fridlund, M., Barragán, O., et al. 2018, *A&A*, **618**, A33
- Piskunov, N., & Valenti, J. A. 2017, *A&A*, **597**, A16
- Rasio, F. A., & Ford, E. B. 1996, *Science*, **274**, 954
- Ricker, G. R., Winn, J. N., Vanderspek, R., et al. 2015, *J. Astron. Telescopes Instrum. Syst.*, **1**, 014003
- Ryabchikova, T., Piskunov, N., Kurucz, R. L., et al. 2015, *Phys. Scr.*, **90**, 054005
- Salmon, S. J. A. J., Van Grootel, V., Buldgen, G., Dupret, M. A., & Eggenberger, P. 2021, *A&A*, **646**, A7
- Salvatiere, J., Wiecki, T., & Fomesbeck, C. 2015, arXiv e-prints [arXiv:1507.08050]
- Schanche, N., Hébrard, G., Collier Cameron, A., et al. 2020, *MNRAS*, **499**, 428
- Schlaufman, K. C., & Winn, J. N. 2016, *ApJ*, **825**, 62
- Schmider, F.-X., Abe, L., Agabi, A., et al. 2022, *SPIE Conf. Ser.*, **12182**, 1218220
- Scuflaire, R., Théado, S., Montalbán, J., et al. 2008, *Ap&SS*, **316**, 83
- Sha, L., Vanderburg, A. M., Huang, C. X., et al. 2023, *MNRAS*, **524**, 1113
- Skrutskie, M. F., Cutri, R. M., Stiening, R., et al. 2006, *AJ*, **131**, 1163
- Sotin, C., Grasset, O., & Mocquet, A. 2007, *Icarus*, **191**, 337
- Steffen, J. H., Ragozzine, D., Fabrycky, D. C., et al. 2012, *PNAS*, **109**, 7982
- Storn, R., & Price, K. V. 1997, *J. Glob. Optim.*, **11**, 341
- Terquem, C., & Papaloizou, J. C. B. 2007, *ApJ*, **654**, 1110
- Theano Development Team, T. T. D., Al-Rfou, R., Alain, G., et al. 2016, arXiv e-prints [arXiv:1605.02688]
- Thiabaud, A., Marboeuf, U., Alibert, Y., et al. 2014, *A&A*, **562**, A27
- Thiabaud, A., Marboeuf, U., Alibert, Y., Leya, I., & Mezger, K. 2015, *A&A*, **574**, A138
- Tinetti, G., Drossart, P., Eccleston, P., et al. 2018, *Exp. Astron.*, **46**, 135
- Tokovinin, A., Fischer, D. A., Bonati, M., et al. 2013, *PASP*, **125**, 1336
- Tommasini, D., & Olivieri, D. N. 2021, *MNRAS*, **506**, 1889
- Valenti, J. A., & Piskunov, N. 1996, *A&AS*, **118**, 595
- Vick, M., Lai, D., & Anderson, K. R. 2019, *MNRAS*, **484**, 5645
- Vick, M., Su, Y., & Lai, D. 2023, *ApJ*, **943**, L13
- Virtanen, P., Gommers, R., Oliphant, T. E., et al. 2020, *Nature Methods*, **17**, 261
- Weidenschilling, S. J., & Davis, D. R. 1985, *Icarus*, **62**, 16
- Wright, E. L., Eisenhardt, P. R. M., Mainzer, A. K., et al. 2010, *AJ*, **140**, 1868
- Wu, D.-H., Wang, S., Zhou, J.-L., Steffen, J. H., & Laughlin, G. 2018, *AJ*, **156**, 96
- Yee, S. W., Petigura, E. A., & von Braun, K. 2017, *ApJ*, **836**, 77
- Zechmeister, M., & Kürster, M. 2009, *A&A*, **496**, 577
- Zeng, L., Jacobsen, S. B., Sasselov, D. D., et al. 2019, *PNAS*, **116**, 9723
- Zhu, W., Dai, F., & Masuda, K. 2018, *RNAAS*, **2**, 160
- ⁷ Centre for Exoplanet Science, SUPA School of Physics and Astronomy, University of St Andrews, North Haugh, St Andrews KY16 9SS, UK
- ⁸ European Space Agency (ESA), European Space Research and Technology Centre (ESTEC), Keplerlaan 1, 2201 AZ Noordwijk, The Netherlands
- ⁹ Department of Space, Earth and Environment, Chalmers University of Technology, Onsala Space Observatory, 439 92 Onsala, Sweden
- ¹⁰ Space Research Institute, Austrian Academy of Sciences, Schmiedlstrasse 6, 8042 Graz, Austria
- ¹¹ Department of Physics, University of Warwick, Gibbet Hill Road, Coventry CV4 7AL, UK
- ¹² CFisUC, Departamento de Física, Universidade de Coimbra, 3004-516 Coimbra, Portugal
- ¹³ Dipartimento di Fisica, Università degli Studi di Torino, via Pietro Giuria 1, 10125, Torino, Italy
- ¹⁴ Dipartimento di Fisica e Astronomia "Galileo Galilei", Università degli Studi di Padova, Vicolo dell'Osservatorio 3, 35122 Padova, Italy
- ¹⁵ Laboratoire Lagrange, UMR7293, Observatoire de la Côte d'Azur, Université Côte d'Azur, Boulevard de l'Observatoire CS 34229 06304 Nice Cedex, France
- ¹⁶ School of Physics and Astronomy, University of Birmingham, Edgbaston, Birmingham B15 2TT, UK
- ¹⁷ Center for Space and Habitability, University of Bern, Gesellschaftsstrasse 6, 3012 Bern, Switzerland
- ¹⁸ Instituto de Astrofísica de Canarias, Vía Láctea s/n, 38200 La Laguna, Tenerife, Spain
- ¹⁹ Departamento de Astrofísica, Universidad de La Laguna, Astrofísico Francisco Sanchez s/n, 38206 La Laguna, Tenerife, Spain
- ²⁰ Admatis, 5. Kandó Kálmán Street, 3534 Miskolc, Hungary
- ²¹ Depto. de Astrofísica, Centro de Astrobiología (CSIC-INTA), ESAC campus, 28692 Villanueva de la Cañada (Madrid), Spain
- ²² Instituto de Astrofísica e Ciências do Espaço, Universidade do Porto, CAUP, Rua das Estrelas, 4150-762 Porto, Portugal
- ²³ Departamento de Física e Astronomia, Faculdade de Ciências, Universidade do Porto, Rua do Campo Alegre, 4169-007 Porto, Portugal
- ²⁴ University of Bern, Sidlerstrasse 5, 3012 Bern, Switzerland
- ²⁵ Institute of Planetary Research, German Aerospace Center (DLR), Rutherfordstrasse 2, 12489 Berlin, Germany
- ²⁶ INAF, Osservatorio Astrofisico di Torino, Via Osservatorio, 20, 10025 Pino Torinese To, Italy
- ²⁷ Centre for Mathematical Sciences, Lund University, Box 118, 221 00 Lund, Sweden
- ²⁸ Aix Marseille Univ, CNRS, CNES, LAM, 38 rue Frédéric Joliot-Curie, 13388 Marseille, France
- ²⁹ Astrobiology Research Unit, Université de Liège, Allée du 6 Août 19C, 4000 Liège, Belgium
- ³⁰ Space sciences, Technologies and Astrophysics Research (STAR) Institute, Université de Liège, Allée du 6 Août 19C, 4000 Liège, Belgium
- ³¹ Institute of Astronomy, KU Leuven, Celestijnenlaan 200D, 3001 Leuven, Belgium
- ³² ELTE Gothard Astrophysical Observatory, Szent Imre h. u. 112, 9700 Szombathely, Hungary
- ³³ SRON Netherlands Institute for Space Research, Niels Bohrweg 4, 2333 CA Leiden, The Netherlands
- ³⁴ Centre Vie dans l'Univers, Faculté des sciences, Université de Genève, Quai Ernest-Ansermet 30, 1211 Genève 4, Switzerland
- ³⁵ Leiden Observatory, University of Leiden, PO Box 9513, 2300 RA Leiden, The Netherlands
- ³⁶ National and Kapodistrian University of Athens, Department of Physics, University Campus, Zografos GR-157 84, Athens, Greece
- ³⁷ Department of Astrophysics, University of Vienna, Türkenschanzstrasse 17, 1180 Vienna, Austria
- ³⁸ Institute for Theoretical Physics and Computational Physics, Graz University of Technology, Petersgasse 16, 8010 Graz, Austria
- ³⁹ Konkoly Observatory, Research Centre for Astronomy and Earth Sciences, Konkoly Thege Miklós út 15-17, 1121 Budapest, Hungary

¹ INAF, Osservatorio Astronomico di Padova, Vicolo dell'Osservatorio 5, 35122 Padova, Italy
e-mail: luca.borsato@inaf.it

² ETH Zurich, Department of Physics, Wolfgang-Pauli-Strasse 2, 8093 Zurich, Switzerland

³ Observatoire astronomique de l'Université de Genève, Chemin Pegasi 51, 1290 Versoix, Switzerland

⁴ Weltraumforschung und Planetologie, Physikalisches Institut, University of Bern, Gesellschaftsstrasse 6, 3012 Bern, Switzerland

⁵ Cavendish Laboratory, JJ Thomson Avenue, Cambridge CB3 0HE, UK

⁶ Department of Astronomy, Stockholm University, AlbaNova University Center, 10691 Stockholm, Sweden

- ⁴⁰ ELTE Eötvös Loránd University, Institute of Physics, Pázmány Péter sétány 1/A, 1117 Budapest, Hungary
- ⁴¹ Lund Observatory, Division of Astrophysics, Department of Physics, Lund University, Box 118, 22100 Lund, Sweden
- ⁴² IMCCE, UMR8028 CNRS, Observatoire de Paris, PSL Univ., Sorbonne Univ., 77 av. Denfert-Rochereau, 75014 Paris, France
- ⁴³ Institut d'astrophysique de Paris, UMR7095 CNRS, Université Pierre & Marie Curie, 98bis blvd. Arago, 75014 Paris, France
- ⁴⁴ Astrophysics Group, Lennard Jones Building, Keele University, Staffordshire ST5 5BG, UK
- ⁴⁵ Istituto di Scienze Polari del Consiglio Nazionale delle Ricerche (CNR-ISP), via Torino 155, 30172 Venezia-Mestre, Italy
- ⁴⁶ Programma Nazionale di Ricerche in Antartide (PNRA), Lungotevere Grande Ammiraglio Thaon di Revel 76, 00196 Rome, Italy
- ⁴⁷ INAF, Osservatorio Astrofisico di Catania, Via S. Sofia 78, 95123 Catania, Italy
- ⁴⁸ Institute of Optical Sensor Systems, German Aerospace Center (DLR), Rutherfordstrasse 2, 12489 Berlin, Germany
- ⁴⁹ Institut fuer Geologische Wissenschaften, Freie Universitaet Berlin, Maltheserstrasse 74-100, 12249 Berlin, Germany
- ⁵⁰ Institut de Ciencies de l'Espai (ICE, CSIC), Campus UAB, Can Magrans s/n, 08193 Bellaterra, Spain
- ⁵¹ Institut d'Estudis Espacials de Catalunya (IEEC), 08860 Castelldefels (Barcelona), Spain
- ⁵² HUN-REN-ELTE Exoplanet Research Group, Szent Imre h. u. 112., Szombathely 9700, Hungary
- ⁵³ Institute of Astronomy, University of Cambridge, Madingley Road, Cambridge CB3 0HA, UK

Appendix A: Observations log and results

This appendix contains the tables with the log of photometric observations (Table [A.1](#)), the observed transit times of both planets (Tables [A.2](#) and [A.3](#)), and the best-fit MAP parameter set (Table [A.4](#)) of the photo-dynamical analysis with TRADES, as described in detail in Sec. [4.3](#). The photometry of TESS, CHEOPS, and ASTEP+ with the MAP model is shown in Fig. [A.1](#) and photometric residuals are plotted in Fig. [A.2](#).

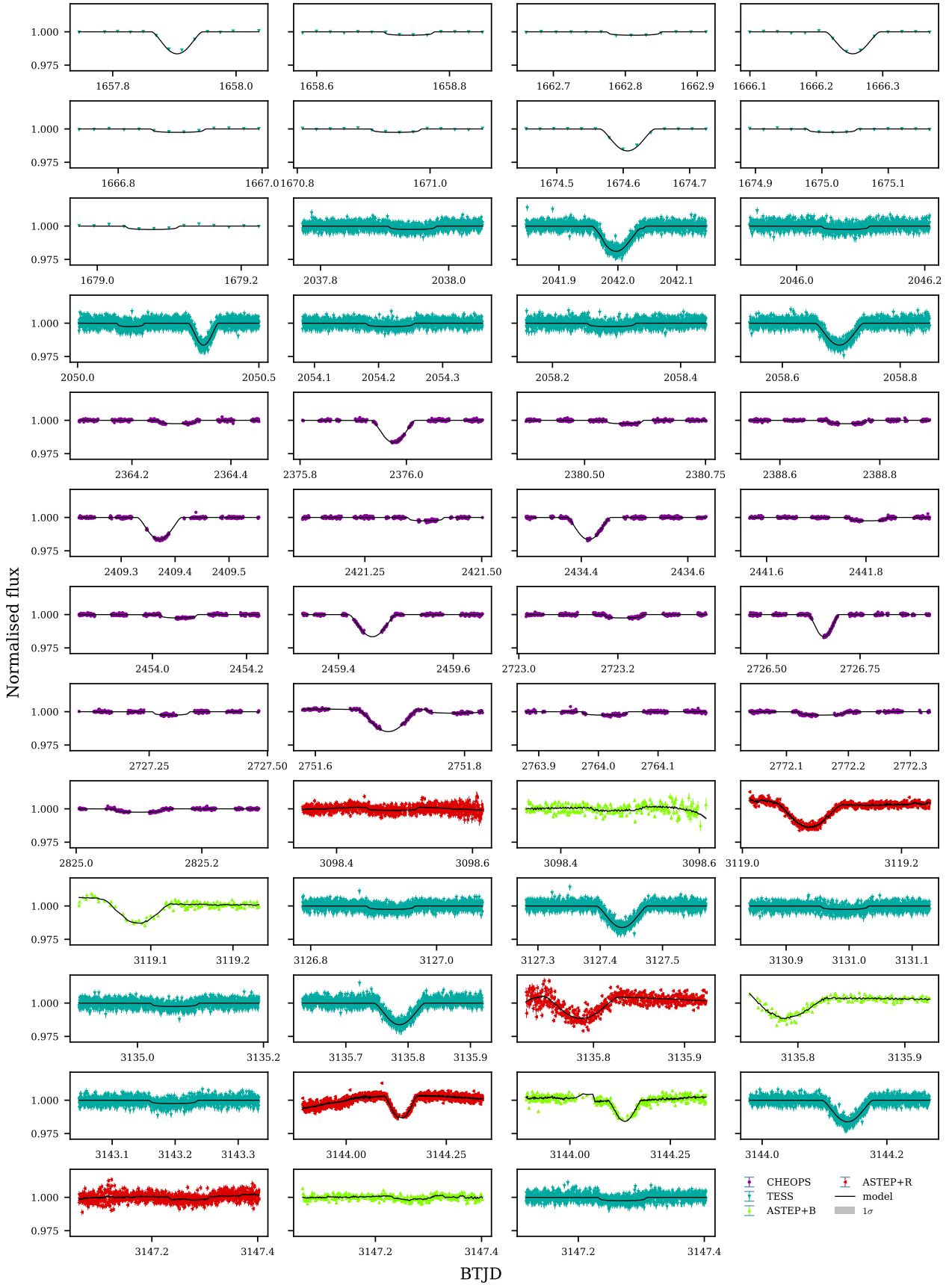


Fig. A.1. Photometry of each light curve used in the photo-dynamical analysis. Each panel has the data (filled markers, different marker and colour based on the facilities, see legend) with error-bars, and the over-plotted (over-sampled) full model (black line, transit and detrending) computed with the MAP parameter set from TRADES. Model uncertainties plotted as grey-shaded area at 1σ , but barely visible. Times in $BTJD = BJD_{TDB} - 2457000$.

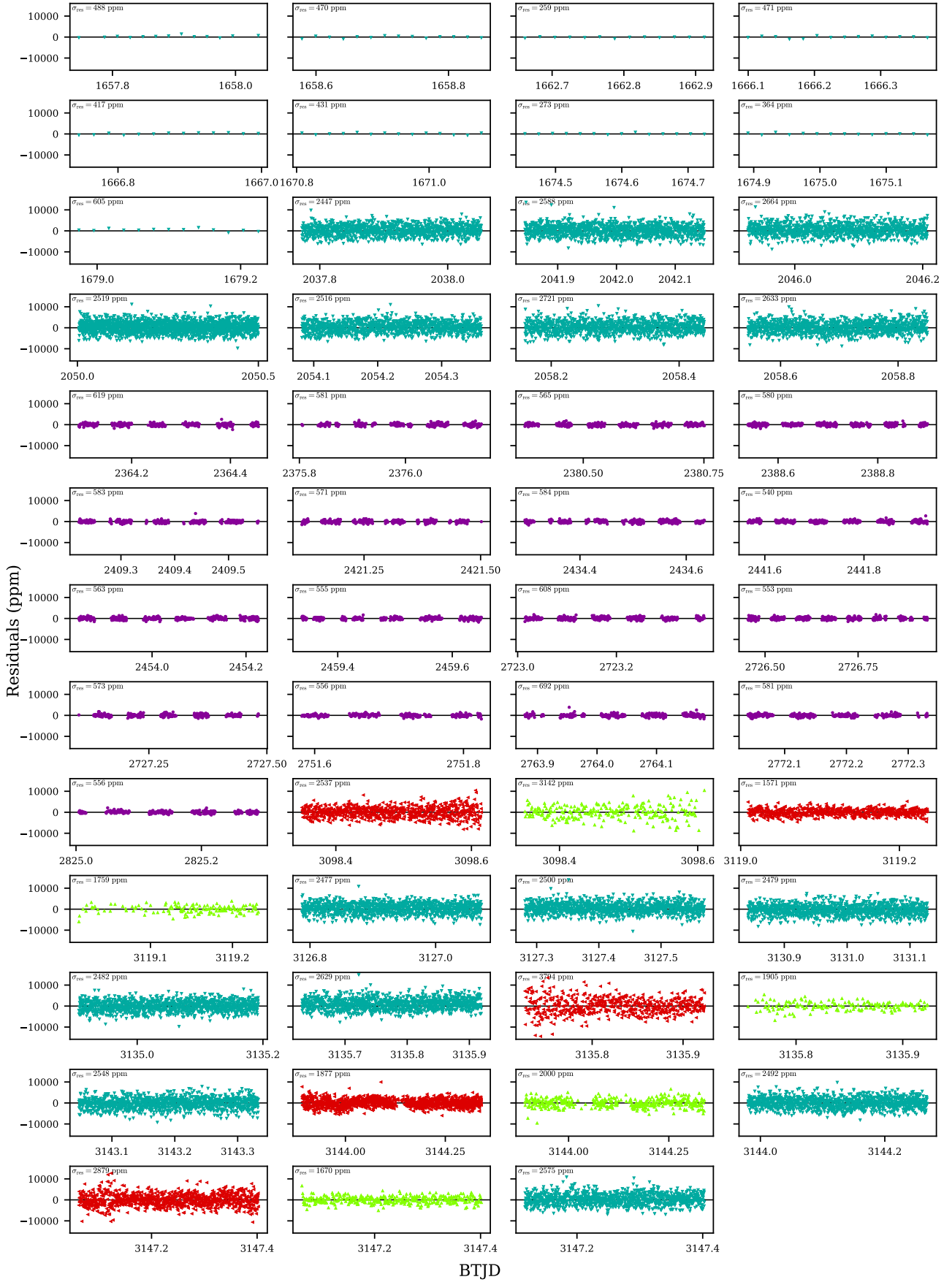


Fig. A.2. As in Fig. A.1, but for the residuals (in ppm) between the observed photometry and the MAP full model. Each panel shows in the upper-left corner the standard deviation of the residuals in ppm.

Table A.1. Log of TOI-1130 observations.

#		DATA ID	Start date (UTC)	Duration (h)	Frames	exp. time (s)	Efficiency (%)	Planet(s)
-	TESS	s0013-0000000254113311	2019-06-19T09:55	-	-	1800	-	b,c
-	TESS	s0027-0000000254113311-0189-a_fast	2020-07-05T18:31	-	-	20	-	b,c
1	CHEOPS	CH_PR100031_TG040601_V0200	2021-05-29T14:06	8.7	260	60	50	b
2	CHEOPS	CH_PR100015_TG018001_V0200	2021-06-10T07:11	8.1	243	60	50	c
3	CHEOPS	CH_PR100031_TG040801_V0200	2021-06-14T20:58	8.9	309	60	58	b
4	CHEOPS	CH_PR100031_TG040802_V0200	2021-06-23T00:44	8.6	291	60	56	b
5	CHEOPS	CH_PR100015_TG018101_V0200	2021-07-13T17:09	8.0	237	60	49	c
6	CHEOPS	CH_PR100031_TG042201_V0200	2021-07-25T14:39	9.2	271	60	49	b
7	CHEOPS	CH_PR100015_TG018201_V0200	2021-08-07T18:59	8.1	246	60	51	c
8	CHEOPS	CH_PR100031_TG044601_V0200	2021-08-15T01:27	8.7	291	60	56	b
9	CHEOPS	CH_PR100031_TG044602_V0200	2021-08-27T08:08	9.2	308	60	56	b
10	CHEOPS	CH_PR100015_TG018301_V0200	2021-09-01T20:00	7.5	239	60	53	c
11	CHEOPS	CH_PR100031_TG052801_V0200	2022-05-23T12:13	8.7	275	60	53	b
12	CHEOPS	CH_PR100015_TG022801_V0200	2022-05-26T22:46	11.6	344	60	50	c
13	CHEOPS	CH_PR100031_TG052901_V0200	2022-05-27T14:17	9.1	247	60	45	b
14	CHEOPS	CH_PR120053_TG004701_V0200	2022-06-21T01:51	5.8	209	60	60	b,c
15	CHEOPS	CH_PR120053_TG004601_V0200	2022-07-03T08:57	7.2	240	60	55	b
16	CHEOPS	CH_PR120053_TG004602_V0200	2022-07-11T12:50	7.0	236	60	56	b
17	CHEOPS	CH_PR120053_TG005101_V0200	2022-09-02T11:59	6.9	222	60	54	b
1	ASTEP+	TOI-1130.02_20230602_B	2023-06-02T20:24	6.2	248	60	-	b
1	ASTEP+	TOI-1130.02_20230602_R	2023-06-02T20:24	6.4	785	20	-	b
2	ASTEP+	TOI-1130.01_20230623_B	2023-06-23T12:18	5.3	135	60	-	c
2	ASTEP+	TOI-1130.01_20230623_R	2023-06-23T12:13	5.4	685	20	-	c
-	TESS	s0067-0000000254113311-0261-a_fast	2023-07-01T03:30	-	-	20	-	b,c
3	ASTEP+	TOI-1130.01_20230709_B	2023-07-10T06:07	4.0	162	60	-	c
3	ASTEP+	TOI-1130.01_20230709_R	2023-07-10T05:25	4.7	593	20	-	c
4	ASTEP+	TOI-1130.01_20230718_B	2023-07-18T09:23	10.7	390	60	-	c
4	ASTEP+	TOI-1130.01_20230718_R	2023-07-18T09:23	10.8	1292	20	-	c
5	ASTEP+	TOI-1130.02_20230721_B	2023-07-21T13:30	8.1	349	60	-	b
5	ASTEP+	TOI-1130.02_20230721_R	2023-07-21T13:30	8.2	1016	20	-	b

Table A.2. Transit times (T_{0s}) of TOI-1130 b.

TOI-1130 b		
$T_{\text{ref}} = 2392.8147 \pm 0.0002(0.0126)$ BTJD _{TDB}		
$P_{\text{lin}} = 4.078668 \pm 0.000002(0.000097)$ days		
T_0	σ_{T_0}	source
1658.73999	0.00710	TESS-S13
1662.81104	0.00306	TESS-S13
1666.88336	0.00576	TESS-S13
1670.95086	0.00478	TESS-S13
1675.01606	0.00486	TESS-S13
1679.07242	0.00529	TESS-S13
1731.94194	0.00091	LCO-SSO
2037.94623	0.00303	TESS-S27
2042.00827	0.00157	TESS-S27
2046.07458	0.00191	TESS-S27
2050.14405	0.00333	TESS-S27
2054.21920	0.00178	TESS-S27
2058.29358	0.00342	TESS-S27
2364.28998	0.00177	CHEOPS
2376.50951	0.00078	LCO-SAAO
2380.58414	0.00589	CHEOPS
2384.66071	0.00081	LCO-CTIO
2388.73347	0.00086	CHEOPS
2392.81083	0.00194	LCO-CTIO
2421.37739	0.00395	CHEOPS
2429.54946	0.00092	LCO-SAAO
2433.63585	0.00075	LCO-CTIO
2441.80478	0.00052	CHEOPS
2454.05512	0.00204	CHEOPS
2723.21209	0.00068	CHEOPS
2727.30096	0.00636	CHEOPS
2751.78779	0.00109	CHEOPS
2764.01177	0.00097	CHEOPS
2772.15663	0.00057	CHEOPS
2825.10022	0.00068	CHEOPS
3098.48272	0.00147	ASTEP+ R
3098.60441	0.00935	ASTEP+ B
3126.92521	0.00192	TESS-S67
3130.99262	0.00143	TESS-S67
3135.05644	0.00261	TESS-S67
3143.19552	0.00168	TESS-S67
3147.26878	0.00374	ASTEP+ R
3147.26951	0.00093	TESS-S67
3147.27052	0.00204	ASTEP+ B

Notes. Linear ephemeris (T_{ref} and P_{lin} with associated uncertainty) from the photometric analysis with PYORBIT as described in Sec. 4.1 and full list of transit times (T_{0s}) of TOI-1130 b.

Table A.3. Transit times (T_{0s}) of TOI-1130 c.

TOI-1130 c		
$T_{\text{ref}} = 2392.66995 \pm 0.00007(0.00218)$ BTJD _{TDB}		
$P_{\text{lin}} = 8.349560 \pm 0.000002(0.000023)$ days		
T_0	σ_{T_0}	source
1657.90383	0.00103	TESS-S13
1666.25464	0.00086	TESS-S13
1674.60532	0.00094	TESS-S13
1758.10894	0.00090	PEST
1975.18610	0.00037	LCO-SSO
2008.58978	0.00054	LCO-SAAO
2041.99674	0.00062	TESS-S27
2050.34671	0.00035	TESS-S27
2058.69699	0.00076	TESS-S27
2067.04526	0.00029	ASTEP, LCO-SSO, PEST
2083.74135	0.00064	CDK14
2092.08823	0.00059	PEST
2317.51746	0.00052	LCO-SAAO
2375.97590	0.00026	CHEOPS
2392.67431	0.00028	LCO-CTIO
2409.37117	0.00029	CHEOPS
2426.06660	0.00037	LCO-SSO
2434.41375	0.00021	CHEOPS
2451.10989	0.00047	ASTEP
2459.45902	0.00018	CHEOPS
2726.65265	0.00025	CHEOPS
2751.69770	0.00021	CHEOPS
3119.08278	0.00035	ASTEP+ R
3119.08399	0.00148	ASTEP+ B
3127.43479	0.00059	TESS-S67
3135.78403	0.00138	ASTEP+ R
3135.78607	0.00070	TESS-S67
3135.78661	0.00233	ASTEP+ B
3144.13645	0.00043	TESS-S67
3144.13705	0.00041	ASTEP+ R
3144.13902	0.00112	ASTEP+ B

Notes. Linear ephemeris and transit times of TOI-1130 c as in Table A.2.

Table A.4. Fitted and physical parameters from the photo-dynamical model with TRADES.

parameters	prior	MAP (HDI 68.27%)	High-precision parameters
stellar parameters			
<i>fitted</i>			
$R_\star (R_\odot)$	$\mathcal{G}(0.697, 0.011)$	$0.697^{+0.005}_{-0.004}$	0.697
$\rho_\star (\rho_\odot)$	$\mathcal{G}(2.13, 0.16)$	$2.20^{+0.04}_{-0.04}$	
LD $q_{1,\text{CHEOPS}}$	$\mathcal{U}(0, 1)$	$0.50^{+0.07}_{-0.03}$	
LD $q_{2,\text{CHEOPS}}$	$\mathcal{U}(0, 1)$	$0.21^{+0.06}_{-0.11}$	
LD $q_{1,\text{TESS}}$	$\mathcal{U}(0, 1)$	$0.50^{+0.05}_{-0.07}$	
LD $q_{2,\text{TESS}}$	$\mathcal{U}(0, 1)$	$0.27^{+0.12}_{-0.09}$	
LD $q_{1,\text{ASTEP+B}}$	$\mathcal{U}(0, 1)$	$0.38^{+0.06}_{-0.05}$	
LD $q_{2,\text{ASTEP+B}}$	$\mathcal{U}(0, 1)$	$0.7^{+0.1}_{-0.2}$	
LD $q_{1,\text{ASTEP+R}}$	$\mathcal{U}(0, 1)$	$0.1959^{+0.0859}_{-0.0010}$	
LD $q_{2,\text{ASTEP+R}}$	$\mathcal{U}(0, 1)$	$0.8^{+0.1}_{-0.5} (2\sigma)$	
<i>physical</i>			
$M_\star (M_\odot)$	-	$0.745^{+0.007}_{-0.009}$	0.745
LD $u_{1,\text{CHEOPS}}$	$\mathcal{G}(0.53, 0.04)$	$0.30^{+0.08}_{-0.13}$	
LD $u_{2,\text{CHEOPS}}$	$\mathcal{G}(0.12, 0.07)$	$0.41^{+0.17}_{-0.09}$	
LD $u_{1,\text{TESS}}$	$\mathcal{G}(0.66, 0.05)$	$0.4^{+0.2}_{-0.1}$	
LD $u_{2,\text{TESS}}$	$\mathcal{G}(0.06, 0.09)$	$0.3^{+0.1}_{-0.2}$	
LD $u_{1,\text{ASTEP+B}}$	$\mathcal{G}(0.37, 0.10)$	$0.8^{+0.2}_{-0.1}$	
LD $u_{2,\text{ASTEP+B}}$	$\mathcal{G}(0.25, 0.10)$	$-0.2^{+0.2}_{-0.2}$	
LD $u_{1,\text{ASTEP+R}}$	$\mathcal{G}(0.37, 0.10)$	$0.70^{+0.01}_{-0.27}$	
LD $u_{2,\text{ASTEP+R}}$	$\mathcal{G}(0.25, 0.10)$	$-0.3^{+0.5}_{-0.1} (2\sigma)$	
planet b			
<i>fitted</i>			
$\log_{10}(M_b/M_\star)$	$\mathcal{U}(-6.1, -3.1)$	$-4.097^{+0.002}_{-0.003}$	
R_b/R_\star	$\mathcal{U}(0.00048, 1.71394)$	$0.0480^{+0.0002}_{-0.0003}$	
P_b (days)	$\mathcal{U}(3.074, 5.074)$	$4.074554^{+0.000001}_{-0.000441} (2\sigma)$	4.074554
$\sqrt{e} \cos \omega_b$	$\mathcal{U}(-0.5, 0.5)$	$-0.17777^{+0.00003}_{-0.00259} (2\sigma)$	
$\sqrt{e} \sin \omega_b$	$\mathcal{U}(-0.5, 0.5)$	$0.1434^{+0.0005}_{-0.0003}$	
λ_b ($^\circ$) ²⁴	$\mathcal{U}(0, 360)$	$120.81^{+0.13}_{-0.04} (2\sigma)$	
i_b ($^\circ$)	$\mathcal{U}(70, 120)$	$87.49^{+0.02}_{-0.08}$	87.494901
<i>physical</i>			
$M_b (M_\oplus)$	-	$19.8^{+0.2}_{-0.3}$	19.833346
K_b (m s^{-1})	-	$9.67^{+0.05}_{-0.08}$	
$R_b (R_\oplus)$	-	$3.66^{+0.03}_{-0.04}$	3.657
$\rho_b (\rho_\oplus)$	-	$0.41^{+0.01}_{-0.01}$	
ρ_b (g cm^{-3})	-	$2.23^{+0.06}_{-0.06}$	
a_b (au)	-	$0.0453^{+0.0001}_{-0.0002}$	0.045262
e_b	$\mathcal{U}(0, 0.25)$	$0.052162^{+0.000956}_{-0.000002} (2\sigma)$	0.052162
ω_b ($^\circ$)	-	$141.11^{+0.47}_{-0.09} (2\sigma)$	141.111127
\mathcal{M}_b ($^\circ$)	-	$159.7^{+0.1}_{-0.4} (2\sigma)$	159.696701
Ω_b ($^\circ$)	180 fixed	-	
$T_{\text{eq},1,b}$ ²⁵ (K)	-	825^{+23}_{-23}	
TSM _{1,b} ²⁶	-	83^{+5}_{-5}	

²⁴ λ is the mean longitude, given by the sum of argument of periastron ω , mean anomaly \mathcal{M} , and longitude of ascending node Ω .²⁵ Equilibrium Temperature with T_{eq} with $A_B = 0$ and $f = 1$.²⁶ Transmission Spectroscopic Metric from [Kempton et al. \(2018\)](#) with T_{eq} with Bond albedo $A_B = 0$ and $f = 1$.

Table A.4. continued.

parameters	prior	MAP (HDI 68.27%)	High-precision parameters
$T_{\text{eq},2,b}$ ²⁷ (K)	-	982^{+28}_{-27}	
$\text{TSM}_{2,b}$ ²⁸	-	98^{+6}_{-6}	
planet c			
<i>fitted</i>			
$\log_{10}(M_c/M_\star)$	$\mathcal{U}(-4.87, -1.87)$	$-2.8687^{+0.0002}_{-0.0025} (2\sigma)$	
R_c/R_\star	$\mathcal{U}(0.00048, 1.71394)$	$0.171^{+0.005}_{-0.005}$	
P_c (days)	$\mathcal{U}(7.35, 9.35)$	$8.3501898^{+0.0000938}_{-0.0000010} (2\sigma)$	8.3501898
$\sqrt{e} \cos \omega_c$	$\mathcal{U}(-0.5, 0.5)$	$-0.1992^{+0.0004}_{-0.0022} (2\sigma)$	
$\sqrt{e} \sin \omega_c$	$\mathcal{U}(-0.5, 0.5)$	$-0.009^{+0.002}_{-0.001}$	
λ_c (°)	$\mathcal{U}(0, 360)$	$235.56^{+0.04}_{-0.04}$	
i_c (°)	$\mathcal{U}(70, 120)$	$87.61^{+0.04}_{-0.04}$	87.613475
Ω_c (°)	$\mathcal{U}(0, 360)$	$179.99^{+0.03}_{-0.10} (2\sigma)$	179.993043
<i>physical</i>			
$M_c (M_\oplus)$	-	336^{+2}_{-5}	335.603435
$K_c (m s^{-1})$	-	$128.59^{+0.01}_{-0.80}$	
$R_c (R_\oplus)$	-	$13.0^{+0.4}_{-0.4}$	12.983016
$\rho_c (\rho_\oplus)$	-	$0.15^{+0.01}_{-0.02}$	
$\rho_c (g cm^{-3})$	-	$0.84^{+0.08}_{-0.09}$	
a_c (au)	-	$0.0731^{+0.0002}_{-0.0003}$	0.073056
e_c	$\mathcal{U}(0, 0.25)$	$0.0398^{+0.0009}_{-0.0002} (2\sigma)$	0.039773
ω_c (°)	-	$182.5^{+0.4}_{-0.5}$	182.502357
\mathcal{M}_c (°)	-	$233.1^{+0.5}_{-0.3}$	233.068994
$T_{\text{eq},1,c}$ (K)	-	650^{+18}_{-18}	
$\text{TSM}_{1,c}$	-	135^{+18}_{-17}	
$T_{\text{eq},2,c}$ (K)	-	773^{+22}_{-21}	
$\text{TSM}_{2,c}$	-	160^{+21}_{-20}	
radial velocities			
<i>fitted</i>			
$\gamma_{\text{CHIRON}} (m s^{-1})$	$\mathcal{U}(-10567, -8567)$	-9568^{+4}_{-4}	
$\gamma_{\text{HARPS}} (m s^{-1})$	$\mathcal{U}(-9023, -7023)$	-8023^{+3}_{-1}	
$\gamma_{\text{PFS}} (m s^{-1})$	$\mathcal{U}(-960, -1040)$	$39.8^{+2.7}_{-0.9}$	
$\log_2 \sigma_{\text{jitter,CHIRON}}$	$\mathcal{U}(-13.29, 6.64)$	$0.1^{+0.2}_{-10.3}$	
$\log_2 \sigma_{\text{jitter,HARPS}}$	$\mathcal{U}(-13.29, 6.64)$	$1.3^{+0.2}_{-0.2}$	
$\log_2 \sigma_{\text{jitter,PFS}}$	$\mathcal{U}(-13.29, 6.64)$	$1.31^{+0.38}_{-0.05}$	
RV linear trend ($m s^{-1}/d$)	$\mathcal{U}(-1, 1)$	$0.486^{+0.009}_{-0.026}$	
<i>physical</i>			
$\sigma_{\text{jitter,CHIRON}} (m s^{-1})$	-	$1^{+6}_{-1} (2\sigma)$	
$\sigma_{\text{jitter,HARPS}} (m s^{-1})$	-	$2.5^{+0.3}_{-0.3}$	
$\sigma_{\text{jitter,PFS}} (m s^{-1})$	-	$2.5^{+0.7}_{-0.1}$	
CHEOPS photometry			
<i>fitted</i>			
$f_{14} \text{ const.}$ ²⁹	$\mathcal{U}(0.5, 1.5)$	$1.0043^{+0.0005}_{-0.0024} (2\sigma)$	
df_{14}/dt	$\mathcal{U}(-1, 1)$	$-0.0015^{+0.0004}_{-0.0004}$	
df_{14}/dx	$\mathcal{U}(-1, 1)$	$0.0008^{+0.0001}_{-0.0003} (2\sigma)$	
$d^2 f_{14}/dx^2$	$\mathcal{U}(-1, 1)$	$0.00070^{+0.00001}_{-0.00034}$	
df_{14}/dy	$\mathcal{U}(-1, 1)$	$-0.0005^{+0.0001}_{-0.0001}$	

²⁷ Equilibrium Temperature T_{eq} with $A_B = 0$ and $f = 2$.²⁸ Transmission Spectroscopic Metric (TSM) from [Kempton et al. \(2018\)](#) with T_{eq} with $A_B = 0$ and $f = 2$.²⁹ f stands for the normalised flux.

Table A.4. continued.

parameters	prior	MAP (HDI 68.27%)	High-precision parameters
$d^2 f_{14}/dy^2$	$\mathcal{U}(-1, 1)$	$0.00034^{+0.00001}_{-0.00027}$	
$d^2 f_{14}/dxdy$	$\mathcal{U}(-1, 1)$	$-0.0005^{+0.0003}_{-0.0002}$	
df_{14}/dbg	$\mathcal{U}(-1, 1)$	$-0.00086^{+0.00072}_{-0.00006}$	
$df_{14}/d \cos \phi^{30}$	$\mathcal{U}(-1, 1)$	$0.0035^{+0.0008}_{-0.0036} (2\sigma)$	
$df_{14}/d \sin \phi$	$\mathcal{U}(-1, 1)$	$-0.0014^{+0.0015}_{-0.0004} (2\sigma)$	
$df_{14}/d \cos 2\phi$	$\mathcal{U}(-1, 1)$	$0.0016^{+0.0003}_{-0.0016} (2\sigma)$	
$df_{14}/d \sin 2\phi$	$\mathcal{U}(-1, 1)$	$-0.0016^{+0.0016}_{-0.0004} (2\sigma)$	
$df_{14}/d \cos 3\phi$	$\mathcal{U}(-1, 1)$	$0.000233^{+0.000004}_{-0.000239}$	
$df_{14}/d \sin 3\phi$	$\mathcal{U}(-1, 1)$	$-0.0007^{+0.0007}_{-0.0002} (2\sigma)$	
ASTEP+ B photometry			
<i>fitted</i>			
f_1 const.	$\mathcal{U}(0.5, 1.5)$	$1.0066^{+0.0002}_{-0.0008}$	
df_1/dt	$\mathcal{U}(-1, 1)$	$-0.062^{+0.011}_{-0.003}$	
$d^2 f_1/dt^2$	$\mathcal{U}(-1, 1)$	$0.161^{+0.009}_{-0.039}$	
df_1/dx	$\mathcal{U}(-1, 1)$	$-0.00015^{+0.00006}_{-0.00007}$	
df_1/dy	$\mathcal{U}(-1, 1)$	$0.0003^{+0.0001}_{-0.0002}$	
$df_1/dfwhm$	$\mathcal{U}(-1, 1)$	$0.00033^{+0.00022}_{-0.00003}$	
$df_1/dsky$	$\mathcal{U}(-1, 1)$	$0.00013^{+0.00004}_{-0.00014}$	
f_2 const.	$\mathcal{U}(0.5, 1.5)$	$1.0036^{+0.0002}_{-0.0007}$	
df_2/dt	$\mathcal{U}(-1, 1)$	$0.019^{+0.015}_{-0.004}$	
$d^2 f_2/dt^2$	$\mathcal{U}(-1, 1)$	$-0.13^{+0.01}_{-0.07}$	
df_2/dx	$\mathcal{U}(-1, 1)$	$-0.000449^{+0.000002}_{-0.000078}$	
df_2/dy	$\mathcal{U}(-1, 1)$	$-0.00031^{+0.00007}_{-0.00003}$	
$df_2/dfwhm$	$\mathcal{U}(-1, 1)$	$-0.00032^{+0.00005}_{-0.00008}$	
$df_2/dsky$	$\mathcal{U}(-1, 1)$	$0.0011^{+0.0001}_{-0.0002}$	
f_3 const.	$\mathcal{U}(0.5, 1.5)$	$1.0004^{+0.0002}_{-0.0002}$	
df_3/dt	$\mathcal{U}(-1, 1)$	$-0.009^{+0.001}_{-0.002}$	
$d^2 f_3/dt^2$	$\mathcal{U}(-1, 1)$	$0.037^{+0.004}_{-0.002}$	
df_3/dx	$\mathcal{U}(-1, 1)$	$-0.00049^{+0.00012}_{-0.00001}$	
df_3/dy	$\mathcal{U}(-1, 1)$	$-0.00101^{+0.00004}_{-0.00010}$	
$df_3/dfwhm$	$\mathcal{U}(-1, 1)$	$0.00022^{+0.00003}_{-0.00007}$	
$df_3/dsky$	$\mathcal{U}(-1, 1)$	$-0.00007^{+0.00007}_{-0.00005}$	
f_4 const.	$\mathcal{U}(0.5, 1.5)$	$0.9993^{+0.0002}_{-0.0003}$	
df_4/dt	$\mathcal{U}(-1, 1)$	$0.012^{+0.007}_{-0.005}$	
$d^2 f_4/dt^2$	$\mathcal{U}(-1, 1)$	$-0.01^{+0.03}_{-0.03}$	
df_4/dx	$\mathcal{U}(-1, 1)$	$0.00047^{+0.00003}_{-0.00015}$	
df_4/dy	$\mathcal{U}(-1, 1)$	$0.000011^{+0.000008}_{-0.000165}$	
$df_4/dfwhm$	$\mathcal{U}(-1, 1)$	$0.00011^{+0.00003}_{-0.00021}$	
$df_4/dsky$	$\mathcal{U}(-1, 1)$	$-0.0011^{+0.0002}_{-0.0003}$	
f_5 const.	$\mathcal{U}(0.5, 1.5)$	$0.9998^{+0.0004}_{-0.0001} (2\sigma)$	
df_5/dt	$\mathcal{U}(-1, 1)$	$0.003^{+0.002}_{-0.009} (2\sigma)$	
$d^2 f_5/dt^2$	$\mathcal{U}(-1, 1)$	$0.003^{+0.029}_{-0.008} (2\sigma)$	
df_5/dx	$\mathcal{U}(-1, 1)$	$0.00014^{+0.00005}_{-0.00003}$	
df_5/dy	$\mathcal{U}(-1, 1)$	$-0.00002^{+0.00003}_{-0.00013} (2\sigma)$	
$df_5/dfwhm$	$\mathcal{U}(-1, 1)$	$0.000367^{+0.000067}_{-0.000008}$	
$df_5/dsky$	$\mathcal{U}(-1, 1)$	$-0.00057^{+0.00007}_{-0.00030} (2\sigma)$	
ASTEP+ R photometry			

³⁰ ϕ is the CHEOPS roll angle.

Table A.4. continued.

parameters	prior	MAP (HDI 68.27%)	High-precision parameters
<i>fitted</i>			
f_1 const.	$\mathcal{U}(0.5, 1.5)$	$1.0053^{+0.0003}_{-0.0001}$	
df_1/dt	$\mathcal{U}(-1, 1)$	$-0.036^{+0.002}_{-0.005}$	
d^2f_1/dt^2	$\mathcal{U}(-1, 1)$	$0.15^{+0.01}_{-0.01}$	
df_1/dx	$\mathcal{U}(-1, 1)$	$0.000213^{+0.000010}_{-0.000064}$	
df_1/dy	$\mathcal{U}(-1, 1)$	$0.000146^{+0.000077}_{-0.000007}$	
$df_1/dfwhm$	$\mathcal{U}(-1, 1)$	$0.00064^{+0.00005}_{-0.00020}$ (2σ)	
$df_1/dsky$	$\mathcal{U}(-1, 1)$	$-0.000080^{+0.000007}_{-0.000134}$	
f_2 const.	$\mathcal{U}(0.5, 1.5)$	$1.0069^{+0.0002}_{-0.0005}$	
df_2/dt	$\mathcal{U}(-1, 1)$	$-0.028^{+0.011}_{-0.004}$	
d^2f_2/dt^2	$\mathcal{U}(-1, 1)$	$-0.00^{+0.02}_{-0.05}$	
df_2/dx	$\mathcal{U}(-1, 1)$	$-0.00010^{+0.00004}_{-0.00007}$	
df_2/dy	$\mathcal{U}(-1, 1)$	$-0.000080^{+0.000114}_{-0.000007}$	
$df_2/dfwhm$	$\mathcal{U}(-1, 1)$	$0.000233^{+0.000007}_{-0.000147}$	
$df_2/dsky$	$\mathcal{U}(-1, 1)$	$-0.00090^{+0.00007}_{-0.00023}$	
f_3 const.	$\mathcal{U}(0.5, 1.5)$	$0.9949^{+0.0001}_{-0.0001}$	
df_3/dt	$\mathcal{U}(-1, 1)$	$0.058^{+0.001}_{-0.001}$	
d^2f_3/dt^2	$\mathcal{U}(-1, 1)$	$-0.101^{+0.002}_{-0.003}$	
df_3/dx	$\mathcal{U}(-1, 1)$	$-0.00038^{+0.00007}_{-0.00001}$	
df_3/dy	$\mathcal{U}(-1, 1)$	$0.00046^{+0.00005}_{-0.00004}$	
$df_3/dfwhm$	$\mathcal{U}(-1, 1)$	$0.00017^{+0.00005}_{-0.00001}$	
$df_3/dsky$	$\mathcal{U}(-1, 1)$	$0.000138^{+0.000059}_{-0.000004}$	
f_4 const.	$\mathcal{U}(0.5, 1.5)$	$0.9985^{+0.0007}_{-0.0002}$ (2σ)	
df_4/dt	$\mathcal{U}(-1, 1)$	$0.048^{+0.005}_{-0.016}$ (2σ)	
d^2f_4/dt^2	$\mathcal{U}(-1, 1)$	$-0.183^{+0.041}_{-0.001}$	
df_4/dx	$\mathcal{U}(-1, 1)$	$-0.00016^{+0.00023}_{-0.00002}$ (2σ)	
df_4/dy	$\mathcal{U}(-1, 1)$	$-0.00025^{+0.00011}_{-0.00004}$	
$df_4/dfwhm$	$\mathcal{U}(-1, 1)$	$0.00001^{+0.00001}_{-0.00009}$	
$df_4/dsky$	$\mathcal{U}(-1, 1)$	$0.0001^{+0.0001}_{-0.0002}$	
f_5 const.	$\mathcal{U}(0.5, 1.5)$	$0.99852^{+0.00006}_{-0.00037}$	
df_5/dt	$\mathcal{U}(-1, 1)$	$0.022^{+0.005}_{-0.002}$	
d^2f_5/dt^2	$\mathcal{U}(-1, 1)$	$-0.045^{+0.008}_{-0.014}$	
df_5/dx	$\mathcal{U}(-1, 1)$	$0.00019^{+0.00005}_{-0.00020}$ (2σ)	
df_5/dy	$\mathcal{U}(-1, 1)$	$-0.00011^{+0.00002}_{-0.00015}$	
$df_5/dfwhm$	$\mathcal{U}(-1, 1)$	$-0.00022^{+0.00007}_{-0.00003}$	
$df_5/dsky$	$\mathcal{U}(-1, 1)$	$0.00044^{+0.00014}_{-0.00002}$	

Notes. Parameters as Maximum a Posteriori (MAP) and error as High Density Interval (HDI) at 68.27%, if the MAP is out-of HDI 68.27% the HDI at 95.44% is reported and indicated as 2σ . Last column shows the high-precision values of the principal parameters required for a precise N-body integration of the orbits. Osculating parameters at reference time $t_{\text{epoch}} = 2\,458\,657\text{BJD}_{\text{TDB}}$.